~~A~~ Profile-based Estimated Inversion Strength

Zhenquan Wang[1], Jian Yuan[1, *], Robert Wood[2, *], Yifan Chen[1] and Tiancheng Tong[3]

[1] School of Atmospheric Sciences, Nanjing University, Nanjing, China

[2] Department of Atmospheric Science, University of Washington, Seattle, USA

[3] Tianwen School, Yichang, China

Correspondence to: Jian Yuan (jiany@nju.edu.cn) and Robert Wood (robwood2@uw.edu)

Abstract. To better measure the planetary boundary layer inversion strength (IS), a novel profile-based method of estimated inversion strength (EIS$_p$) is developed using the ERA5 daily reanalysis data. The EIS$_p$ is designed to estimate the IS based on the thinnest possible reanalysis layer above the lifting condensation level encompassing the inversion layer. At ~~the Southern Great Plains site~~a ground-based site in south America, the EIS$_p$ better correlates with the radiosonde-detected IS (R=0.74) than the lower-tropospheric stability (LTS, R=0.53) and the estimated inversion strength (EIS, R=0.45). And the daily variance in low-cloud cover (LCC) explained by the EIS$_p$ is twice that explained by the LTS and EIS. Higher correlations between the EIS$_p$ and the radiosonde-detected IS are also found at ~~worldwide~~ other radiosonde stations of subtropics and midlatitude.

Analysis of LCC observed by geostationary satellites and the Moderate Resolution Imaging Spectroradiometer shows that the EIS$_p$ explains 78% of the annual mean LCC spatial variance over global oceans and land, larger than that explained by the LTS/EIS (48%/13%). Over tropical and subtropical low-cloud prevailing eastern oceans, LCC range is more resolved by the EIS$_p$ (48%) than the LTS/EIS (37%/36%). And the EIS$_p$ explains a larger fraction (32%) in the daily LCC variance, as compared to that explained by the LTS/EIS (14%/16%). The seasonal LCC variance explained by the EIS$_p$ is 89%, larger than that explained by the LTS/EIS (80%/70%). The LCC-EIS$_p$ relationship ~~between EIS$_p$ and LCC~~ is more uniform across various time scales than the LCC-LTS/EIS relationship. It is suggested that the EIS$_p$ is a better cloud controlling factor for LCC and likely a useful external environmental constraint for process-level studies in which there is a need to control for large-scale meteorology in order to isolate the cloud responses to aerosols on short timescales.

1. Introduction

The inversion strength (IS) of the planetary boundary layer (PBL) is an important factor affecting PBL moisture trapping and low cloud formation. Strong IS inhibits the dry air above the inversion from being incorporated into the PBL and traps moisture below the inversion to favor greater cloud cover (Wood and Bretherton, 2006; Mauger and Norris, 2010). In contrast, weak IS promotes the drying effect of entrained air from the free troposphere and reduces the PBL moisture to decrease cloud cover (Bretherton and Wyant, 1997; Myers and Norris, 2013). Currently two approximate measures of the IS based on reanalysis data are widely used as meteorological constraints on low cloud cover (LCC): the lower-tropospheric stability (LTS, Klein and Hartmann (1993)) and the estimated inversion strength (EIS, Wood and Bretherton (2006)). They are both defined as a two-level potential temperature (θ) difference between the 700hPa level and the surface but for the EIS the moist adiabatic θ increase above the lifting condensation level (LCL) is removed in addition. The EIS can be combined with the moisture difference between the 700hPa and surface to form a new stability index, the estimated cloud-top entrainment index (ECTEI). The ECTEI and the EIS have similar correlations with LCC on the seasonal time scales (Kawai et al., 2017).

The LTS and EIS are the best known and most widely-used cloud controlling factors to explain LCC variations. Enhanced LTS can moisten PBLs and has been shown to precede LCC changes by about 24-36 hours (Mauger and Norris, 2010; Klein, 1997). Similarly, Myers and Norris (2013) found that the EIS is the main cause of LCC variations and enhanced subsidence actually decreases LCC for the same value of the EIS. This LCC-LTS/EIS relationship is vital for not only separating observational aerosol effects on clouds from meteorological influences (L'ecuyer et al., 2009; Rosenfeld et al., 2019; Murray-Watson and Gryspeerdt, 2022; Coopman et al., 2016) but also estimating low cloud climate feedbacks (Klein et al., 2017; Sherwood et al., 2020). In terms of aerosol-cloud interactions, the LTS and EIS can be used to constrain meteorological influences and thus largely reduce the confounding influence of meteorology to separate aerosol effects on low clouds (Mauger and Norris, 2007; Coopman et al., 2016), since LCC variations are most explained by the LTS/EIS among all of LCC-controlling meteorological factors (Stevens and Brenguier, 2009). Without strong cloud-controlling factors, the confounding influence of meteorology is poorly constrained and over half of the relationship between aerosol optical depth and LCC results from meteorological covariations (Gryspeerdt et al., 2016). Besides, in climate projections, Webb et al. (2012) found that most climate models cannot reproduce the observational LCC-LTS/EIS relationship and thus low cloud feedbacks have the largest spread among climate models. To help constrain future climate projections, the LTS/EIS-induced low cloud feedback can be more accurately estimated by multiplying the observational LCC-LTS/EIS sensitivity by the LTS/EIS changes of climate model projections (Webb et al., 2012; Qu et al., 2014; Myers and Norris, 2016; Klein et al., 2017; Mccoy et al., 2017; Myers et al., 2021; Seethala et al., 2015; Kawai et al., 2017).

Although the LTS/EIS is best correlated with LCC among all meteorological factors, the LTS/EIS only explains a small portion of LCC variance on short time scales. 12% of daily LCC variance are explained by the LTS, but when the monthly means are subtracted from the data only 4.8% of the daily LCC variance are explained by the LTS at the subtropical ocean weather station (OWS) N (Klein, 1997). Similarly, when the monthly means are removed, only 4% of daily LCC variance are explained by the EIS over the typical subtropical eastern oceans (Szoeke et al., 2016). LCC on daily time scales is not as well explained by the LTS/EIS as the LCC on longer time scales. But the LCC sensitivity to LTS/EIS is assumed to be time-scale invariant to estimate the LTS/EIS-induced low cloud feedback and thus leads to some uncertainty (Klein et al., 2017). The explanation for the variant relationship between LCC and LTS/EIS across different time scales is not clear. And it is also not known whether the LTS and EIS can approximate the IS with the same accuracy across different time scales. ~~This is possibly due to IS not being well estimated by the LTS and EIS on short time scales.~~

Grounded on the well-mixed condition, the PBL's thermal structure is relatively simple and both the LTS and EIS are likely good measures of IS. However, the actual PBL thermal stratification may not always be well-mixed. In deep decoupled PBLs, a strong stratification with a large θ increase between cloud layers and surface-mixed layers would exist (Jones et al., 2011; Nicholls, 1984) ~~θ in the subcloud layer may not be conserved but with a stable layer (Jones et al., 2011)~~. In this case, both the LTS and EIS likely count the stable layers of the decoupling~~within the PBL~~ into the IS estimates and thus overestimate the real IS atop the PBL. Previous studies also showed that the free-tropospheric lapse rate has small biases and large spreads although on average it is close to the moist adiabat on daily time scales (Wood and Bretherton, 2006). Thus further refinements on the algorithm of IS estimations are possible if we can reduce the biases and errors resulting from the deviations from the well-mixed conditions. Given the importance of the LTS/EIS for studies of cloud-aerosol interactions and climate predictions, a better measure of the IS can lead to more accurate quantification and increasing confidence in these fields. Based on the previous EIS framework, this study further establishes a profile-based EIS ($\mathrm{EIS_p}$) algorithm to take advantages of the ERA5 reanalysis and thus more accurately estimate the IS.

This paper is laid out as follows: Section 2 briefly describes the observation and reanalysis data and introduces methodologies used in our analysis; section 3 illustrates the development and validation of the new $\mathrm{EIS_p}$; section 4 evaluates the relationship between LCC and $\mathrm{EIS_p}$ at the global scale~~the $\mathrm{EIS_p}$ on estimating the IS and constraining LCC on global scale~~; with conclusions in section 5.

2. Data and methods

Data used in this study includes: (1) high vertical-resolution radiosondes and cloud radar and lidar observations from the ground site of Atmospheric Radiation Measurement (ARM) Program; (2) radiosondes of several subtropical and midlatitude stations from the Integrated Global Radiosonde Archive (IGRA) of the National Oceanic and Atmospheric Administration (NOAA); (3) global satellite observations of LCC; (4) the fifth-generation atmospheric reanalysis from the European Centre for Medium-Range Weather Forecasts (ECMWF). Methodologies of data processing are also introduced.

2.1 Radiosonde and cloud observations at the ~~ARM~~ ground-based sites

Long-term ground-based observations are from two sites of the ARM Program at the Southern Great Plains (SGP) and the Eastern North Atlantic (ENA) (Ackerman and Stokes, 2003). ARM was established by U.S Department of Energy Office of Biological and Environmental Research to provide an observational basis for studying the Earth's climate. At the SGP observatory (97.5°W, 36.6°N and 318m above the sea level) and the ENA observatory (28.1°W, 39.5°N and 30m above the sea level), high-quality radiosondes and cloud radar and lidar observations are provided to validate the new algorithm of EIS$_p$ and investigate the relationship of IS and IS estimates (i.e., LTS, EIS and EIS$_p$) with LCC. However, the ENA is located on Graciosa Island at the midlatitude ocean where low clouds frequently occur but with no inversion (Norris, 1998) so that it is not an ideal site to investigate the relationship of LCC with IS. Thus, the observations at the ENA are only used to validate the accuracy of EIS$_p$ by comparing with the radiosonde-measured IS.

~~The SGP observatory (97.5°W, 36.6°N and 318m above the sea level) is a long-term field measurement site established by the ARM. In this study, t~~The atmospheric temperature, relative humidity (RH) and pressure profiles measured by the SGP balloon-borne sounding system (SONDE) from 2002 to 2011 are used. The sondes at the SGP are launched four times a day at 5:30, 11:30, 17:30, 23:30 coordinated universal time (UTC). To avoid the diurnal-cycle influence on our analysis, only the sondes launched at 17:30 UTC (11:00 local time) are used. At this time, the PBL is relatively more well-mixed by turbulence with more uniform vertical distribution of θ than the other time of a day (Liu and Liang, 2010). The data at different time are also tested and they come to similar results. The precision of the sonde-measured temperature, RH and pressure is 0.1K, 1% and 0.1hPa (Ken, 2001), respectively. Their accuracy is 0.2K, 2% and 0.5hPa, respectively (Ken, 2001). Its vertical resolution is normally about 10 meters from the ground level up to 30km. The sonde temporal resolution is less than 2.5s with 6m/s ascent rate at the 1000hPa level. The θ profile is computed from the sonde temperature and pressure profiles as:

$$\theta = T\left(\frac{1000}{p}\right)^{\frac{R_a}{c_{pa}}}, \quad (1)$$

where R_a is the specific gas constant of dry air; c_{pa} is the specific heat capacity for dry air at constant pressures. T and p are the sonde temperature and pressure. The θ vertical gradient ($d\theta/dz$) profile is derived from the θ difference between two adjacent levels:

$$\left(\frac{d\theta}{dz}\right)_{\frac{z_{i+1}+z_i}{2}} = \frac{\theta_{i+1}-\theta_i}{z_{i+1}-z_i}, \quad (2)$$

where z is the height above the ground level (AGL). The subscript "i" indicates the i-th level detected by the sonde.

Cloud profiles are observed every 10s by the 35GHz millimeter wavelength cloud radar ~~(MMCR)~~ and the micro-pulse lidar ~~(MPL)~~ from 2002 to 2011 at the SGP. The ARM best estimate cloud radiation measurement (armbecldrad) product is used (Chen and Xie, 1996), which provides radar and lidar cloud profiles derived from the Active Remote Sensing of Clouds (ARSCL). Its vertical resolution is 45 meters. To match the sonde launched at 17:30 UTC, the hourly segment of cloud measurements during 17:00-18:00 UTC is used. The cloud base/top height of an hourly segment is recognized as the lowest/highest level of cloud layers (non-zero cloud fraction) detected in that hourly segment. In a cloud profile, distinct cloud layers are separated by a minimum distance threshold of 250m (Li et al., 2011). Low clouds are defined as the cloud base height less than 3km and the top height less than 4km. These low clouds are dominated by stratus, stratocumulus, and shallow cumulus clouds (Dong et al., 2005). Segments of solely other types of clouds but no low cloud are excluded in our analysis. Segments that have low clouds but with other clouds aloft are kept. The LCC of an hourly segment is defined as the ratio of the number of cloudy profiles to the total number of profiles in that segment.

These hourly segments are further sorted into three categories: clear sky, coupled cloudy and decoupled cloudy segments. Clear sky segments are those in which no cloud is present within that segment. The coupled/decoupled cloudy segments are segments containing low-clouds in coupled/decoupled PBLs, respectively. A straightforward indicator to distinguish coupled and decoupled PBLs is the height difference between the cloud base and the LCL (Δz_b) (Jones et al., 2011). When the PBL is well mixed, Δz_b is close to zero, but in the decoupled PBLs the cloud and subcloud layers would be separated by a stable layer and the LCL may diverge from the cloud base hundreds of meters with large Δz_b (Nicholls, 1984; Jones et al., 2011). The threshold value of Δz_b is empirical and for different instrument capability, vertical resolution and locations the threshold may be a little different. In reference to the linear least-square fit between Δz_b and $\Delta\theta$ in Jones et al. (2011) that 150 meters of Δz_b correspond to 0.5K of the θ difference in the subcloud layer, a similar linear relationship is found but the slope is a little different that 180 meters of Δz_b corresponds to 0.5K of the θ difference at the SGP site. Thus at the SGP site, a threshold value of 180 meters for Δz_b is used to distinguish coupled and decoupled PBLs.

At the ENA, data of radiosondes and LCC from 2014 to 2020 are used.~~The ARM Eastern North Atlantic (ENA) atmospheric observatory is located on Graciosa Island (28.1°W, 39.5°N).~~ The data product and processing method of the ENA site is the same to that of the SGP. The ENA site is characterized by marine stratocumulus clouds but at midlatitude where the correlation between LCC and IS is much weaker as compared to that at the SGP. This will be verified and discussed later.~~oceans where the relationship between LCC and IS is poor and stratus occurs usually with no inversion (Norris, 1998). Our results will further confirm this at the ENA site latter. In contrast, the SGP is a more suitable site than the ENA to study the relationship between LCC and IS. At the SGP, LCC and IS are better correlated with each other than that at the ENA but this LCC-IS relationship is poorly/wrongly reflected by the LTS and EIS according to our results, which outstands the problem of using the LTS and EIS to estimate the IS. Thus in this study we choose to show detailed analysis based on the observations at the SGP site, while the analysis at the ENA site is summarized and listed together with other radiosonde stations in Table 2.~~

2.2 Radiosonde stations of subtropics and midlatitude ~~Worldwide radiosonde stations~~

The ~~Integrated Global Radiosonde Archive (~~IGRA~~)~~ of ~~the National Oceanic and Atmospheric Administration (~~NOAA~~)~~ collects radiosondes from global distributed stations (Durre et al., 2018; Durre et al., 2006). The radiosonde temperature, RH, pressure, and geopotential height profiles in the IGRA are used. The θ and θ gradient profiles are computed from Eqs. (1) and (2). These atmospheric parameters of radiosondes are available at the standard pressure levels (1000, 925, 850, 700 and 500hPa) or variable levels. It provides reliable instantaneous observations for the PBL IS (see definitions in the section 2.5). However, most low-cloud dominated regions are over the ocean with no available radiosondes in the IGRA. Thus five radiosonde stations with relatively higher occurrence frequencies of low clouds are selected: the OWS N in the subsidence and steady trade wind circulation of the northeast Pacific (Klein, 1997; Klein et al., 1995); the OWS C in the frequently decoupled PBLs of the north Atlantic (Norris, 1998); the tropical east Pacific coast with the classic stratocumulus condition (Albrecht et al., 1995); the southeast Pacific coast with the stratocumulus-capped PBLs (Bretherton et al., 2004) and the southeast Chinese coast of subtropical low-cloud domains (Klein and Hartmann, 1993). Locations, observational period and time of data for each station are listed in Table1.

Table 1. The location, observational period and time of the IGRA radiosonde stations.

	OWS N	OWS C	Tropical East Pacific coast	Southeast Pacific coast	Chinese coast
Location	(140°W, 30°N)	(35.5°W, 52.75°N)	(120.5667°W, 34.75°N)	(70.4408°W, 23.4503°S)	(119.2833°E, 26.0833°N)
Period	1969-1974	1969-1974	2006-2011	2006-2011	2006-2011

Time	00UTC	12UTC	00UTC	12UTC	00UTC

2.3 ~~GEO-MODIS~~Global LCC observations

Global ~~hourly~~ LCC observations of ~~between 60°S and 60°N derived from~~the geostationary satellites (GEOs) and the Moderate Resolution Imaging Spectroradiometer (MODIS) onboard the Aqua and Terra satellites ~~during 2006-2011~~ are provided by the Clouds and the Earth's Radiant Energy System (CERES) project (Doelling et al., 2013; Doelling et al., 2016; Trepte et al., 2019)~~is used~~. Global hourly LCC between 60°S and 60°N during 2006-2011 is used. It is available in the ~~Clouds and the Earth's Radiant Energy System (CERES)~~ synoptic 1-degree (SYN1deg) edition 4.1 product of the CERES project (Doelling et al., 2013; Doelling et al., 2016; Trepte et al., 2019). The GEO-MODIS LCC here refers to the cloud area fraction of the identified cloudy pixels with cloud top pressure above 700hPa divided by the total number of pixels in the 1°×1° grids. The MODIS pixel-level cloud identification is based on the CERES MODIS cloud algorithm (Minnis et al., 2008; Minnis et al., 2011). The sampling frequency of clouds derived from the MODIS narrowband radiance is four times a day (two from each of the Aqua Terra). GEOs with radiances calibrated against the MODIS provide hourly cloud retrievals between MODIS observations (Doelling et al., 2013). The GEO cloudy pixel identification is also based on the CERES MODIS-like cloud algorithm to achieve more uniform MODIS and GEO clouds. An advantage of this product over cloud retrievals of the first-generation GEO is that the CERES project uses the latest generation of the GEO imager capability with more additional channels to enhance the accuracy of cloud retrievals (Doelling et al., 2016). Hourly LCC is used to match the IGRA radiosondes. Daily LCC used in section 4 is the mean of the full-day hourly GEO-MODIS LCC from the CERES SYN1deg Ed4.1 product (Doelling et al., 2016).

2.4 The fifth generation ECMWF atmospheric reanalysis (ERA5)

Reanalysis data from the ECMWF is to provide the atmospheric profile information. The ~~European Centre for Medium-Range Weather Forecasts (ECMWF)~~ ERA5 ~~reanalysis~~ combines observations with model outputs by the 4D-Var assimilation to achieve the 1-hour resolution (Hersbach et al., 2020). The hourly atmospheric temperature, RH, geopotential profiles in the ERA5 dataset are used to match the SGP, IGRA and GEO-MODIS observations. The θ and θ gradient profiles are computed based on Eqs. (1) and (2). Atmospheric profiles at the 16 pressure levels between 500hPa and 1000hPa are available. At the SGP site, the ERA5 atmospheric profiles between the years 2002 and 2011 at the grid point (97.5°W, 36.625°N) nearest to the SGP site (~~away~~ within about 2.8km) is used. For the IGRA radiosonde stations, the ERA5 hourly data of the 0.125° grid point nearest to them during the same observational period is used. At the global scale, the ERA5 atmospheric profiles are averaged to 1° resolution data centered at 0.5 °, 1.5 °, … during the years between 2006 and 2011. This resolution is consistent with the global LCC data. Those three metrics, LTS, EIS and $\mathrm{EIS_p}$, are then computed based on the 3-hour 1° ERA5 atmospheric profiles. All metrices at longer (i.e., from daily to seasonal) time scales are computed from the 3-hour metrices.

2.5 LTS, EIS and radiosonde-measured IS

The LTS and EIS over the ocean are defined as:

$$\mathrm{LTS} = \theta_{700hPa} - \theta_0, \tag{3}$$

$$\mathrm{EIS} = \mathrm{LTS} - \Gamma_m\,(z_{700hPa} - z_{LCL}), \tag{4}$$

where θ and z are, respectively, the potential temperature and the height. The subscripts "700hPa", "0" and "LCL" indicate the levels of 700hPa, 1000hPa and the LCL, respectively. z_{LCL} is calculated using temperature and RH at 1000hPa based on the exact expression in Romps (2017), indicating the height at which an air parcel would saturate if lifted adiabatically. Γ_m is the moist-adiabatic θ gradient at 850hPa calculated using the mean temperature of the 1000hPa and 700hPa levels. Γ_m can be calculated as:

$$\Gamma_m\,(T,p) = (\frac{1000}{p})^{\frac{R_a}{c_{pa}}} \cdot \frac{g}{c_{pa}}(1 - \frac{1+L_v q_s(T,p)/R_a T}{1+L_v^2 q_s(T,p)/c_{pa} R_v T^2}). \qquad (5)$$

q_s is the saturated mass fraction of water vapor. L_v is the latent heat of vaporization. R_v is the specific gas constant for water vapor.

Over land, the LTS and EIS are computed following Eqs. (3)-(5) but based on the heights of 0.15km and 3km AGL. The height of the initial air parcel set as 0.15km AGL is to avoid noisy and contaminated readings of the RH near the surface from the radiosondes and the influence of surface layers (Liu and Liang, 2010). The temperature, RH and pressure at 0.15km and 3km AGL over land can be directly derived from the radiosondes or linearly interpolated from the ERA5 profiles. z_{LCL} over land is calculated using the temperature and RH at 0.15km AGL. Γ_m over land is computed using the mean temperature and pressure of the two heights.

To derive the IS from the radiosonde profiles, the layer of the greatest θ gradient ($d\theta/dz$) between the LCL and 5km AGL is firstly identified, similar to Mohrmann et al. (2019) but with a LCL constraint to guarantee that it is above the cloud layer. For the SGP high-resolution (10 meters) radiosondes, the inversion top/base is ~~thus~~ defined as the nearest level above/below the layer of the maximum $d\theta/dz$ where $d\theta/dz$ equals to three-fourths of the maximum $d\theta/dz$~~height of three-fourths of the greatest $d\theta/dz$ above/below the height of the greatest $d\theta/dz$. An alternative method is to define the layer between the identified height of the greatest $d\theta/dz$ ± 250 meters as the inversion layer. These two methods both works~~. The IS is defined as the θ jumps across the inversion layer after removing the θ increases due to the moist adiabat in this layer:

$$\mathrm{IS} = (\theta_{IST} - \theta_{ISB}) - \Gamma_m^{ISB}(z_{IST} - z_{ISB}). \qquad (6)$$

The subscripts "IST" and "ISB" indicate the identified top and base height of corresponding layers, respectively. Γ_m^{ISB} is the moist-adiabatic $d\theta/dz$ computed from Eq. (5) using the temperature and pressure at the identified inversion base. The method that determines the IS in low-resolution soundings of IGRA is exactly the same as the new profile-based method of EIS and will be introduced in detail in section 3.1.~~For the low-resolution (hundreds of meters) radiosondes in the IGRA, three candidate layers are identified: a layer corresponding to the greatest $d\theta/dz$ above the LCL and this layer combined with an adjacent layer above or below it. The final IS is selected as the maximum diabatic θ increase of the above three candidate layers computed based on Eq. (6).~~

2.6 t-test and multiple timescale analysis

In our study the Pearson's correlation coefficient (R) and the slope of the least-squares linear fit are used. R-square is used with a minus/plus sign for a negative/positive correlation. The existence of a correlation and confidence interval for the true mean value (μ) are estimated based on the t-test. The number of independent samples is determined by dividing the total length of samples by the distance between independent samples (Bretherton et al., 1999). All correlations listed in this study are at the 95% significant level if without a mention of their significance. The confidence bound of R is computed based on the Fisher-Z Transformation. The confidence interval of the slope is computed from the residual error of the least-squares linear fit. Besides, for isolating the correlation and the regression slope on different time scales~~through daily to seasonally~~, window anomalies are defined ~~in~~ as consistent with that in Szoeke et al. (2016):

$$x^{\Delta_i} = [x]^{\Delta_i} - [x]^{\Delta_{i+1}}. \qquad (7)$$

The brackets represent mean of x over the window of length Δ. The superscripts Δ_i and Δ_{i+1} are the i-th window length and the next longer window length. ~~The correlation and slope on the different time scales can be computed from the appropriate window anomalies.~~

3. The profile-based method of EIS (EIS$_p$)

In this section, the new EIS$_p$ algorithm is established based on ground-based observations at the SGP and validated at other radiosonde stations of subtropics and midaltitude. In section 3.1, the new EIS$_p$ algorithm is described. In section 3.2, at the SGP site with long-term 10m-resolution radiosondes, two questions are discussed: (1) why and how is EIS$_p$ a better estimate for the IS than LTS and EIS? (2) how well does EIS$_p$ control LCC as compared to LTS and EIS when it is a better estimate for the IS? In section 3.3, the EIS$_p$ is further validated at radiosonde stations of subtropics and midlatitude.

3.1 The algorithm of the new EIS$_p$

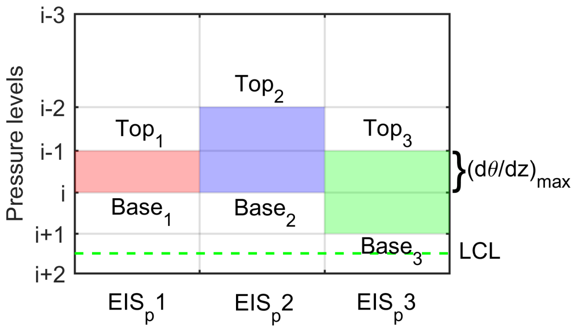

Figure 1. An illustration of finding the location of three possible layers encompassing the inversion between the LCL and 5km AGL in ERA5 or coarse sounding profiles. The red block is one single layer of $(d\theta/dz)_{max}$ that includes the inversion. The blue and green blocks are a combination of two adjacent layers if the inversion is distributed into the two layers but not just in the layer of $(d\theta/dz)_{max}$. EIS$_p$1-3 are computed accordingly and the largest value among them is regarded as the true EIS$_p$.

The EIS$_p$ is designed to capture the IS information from the thinnest layer encompassing the inversion in low-resolution (hundreds of meters) atmospheric profiles. For these coarse-resolution profiles (e.g., ERA5), it is difficult to accurately locate the exact place of the inversion because usually the thickness of the inversion is much smaller than the distance between two adjacent vertical levels. Thus only one or two adjacent layers that could encompass the inversion are located. The latter is for the consideration that an inversion layer may be across two adjacent layers of the ERA5. Specifically, the EIS$_p$ is computed as follows:

(1) *Locating the layer of the maximum θ vertical gradient* $(d\theta/dz)_{max}$:

For each hourly ERA5 profile, the layer of $(d\theta/dz)_{max}$ is firstly located between the LCL and 5km AGL (the red zone in Fig.1), since the inversion just features strong gradients in thermodynamical properties.

(2) *Finding the layers encompassing the full inversion:*

The layer of $(d\theta/dz)_{max}$ may not encompass the full inversion if the inversion crosses two adjacent layers of the ERA5. Thus, the layer of $(d\theta/dz)_{max}$ is combined with an adjacent layer just above and below it respectively, to constitute other two candidate layers that could encompass the full inversion (the blue and green zone in Fig.1).

(3) *Calculating the EIS$_p$:*

The EIS$_p$ is calculated for the three possible layers identified in second stage, respectively:

$$EIS_p = \theta_{top} - \theta_{base} - \Gamma_m(z_{top} - z_{base}), \quad (8)$$

where subscripts "top" and "base" represent the top and base levels of a candidate layer. Γ_m is computed using Eq. (5) at the base level. The θ increase of the moist adiabat is removed to extract the strength of the inversion between the top and base levels, which is consistent with the EIS framework in Wood and Bretherton (2006). The final EIS$_p$ is determined by which layer in Fig.1 encompasses stronger inversion computed from Eq. (8) and thus refers to the largest value among the three candidates EIS$_p$1-3.

The EIS (Wood and Bretherton, 2006) assumes that the PBL is well mixed (dry adiabat below the LCL and moist adiabat above the LCL) for estimating the IS. If that is the case, EIS$_p$ would give the same results as EIS. However, it will be shown in the following sections that the actual PBL often deviates from the well mixed conditions, where the EIS$_p$ provides a physically more reasonable estimate for the IS than the EIS and thus a stronger cloud-controlling factor.

When high-resolution radiosondes are available, the exact IS can be obtained fairly straightforward (section 2.5, Eq. 6). The computation of EIS$_p$ is in fact adapted from the algorithm of obtaining the IS from high-resolution radiosondes, but is adjusted to suit coarse-resolution atmospheric profiles in reanalysis. Because high-resolution soundings are rare, an applicable metric derived from reanalysis would be much more beneficial. Because the IGRA soundings have similar vertical resolutions as ERA5 in lower troposphere, the IS of these soundings (used in section 3.3) is derived exactly by the same way as the EIS$_p$

3.2~~1~~ PBL stratification and the establishment of the EIS$_p$ at the SGP ~~Constraining LCC by LTS, EIS and IS at the SGP~~

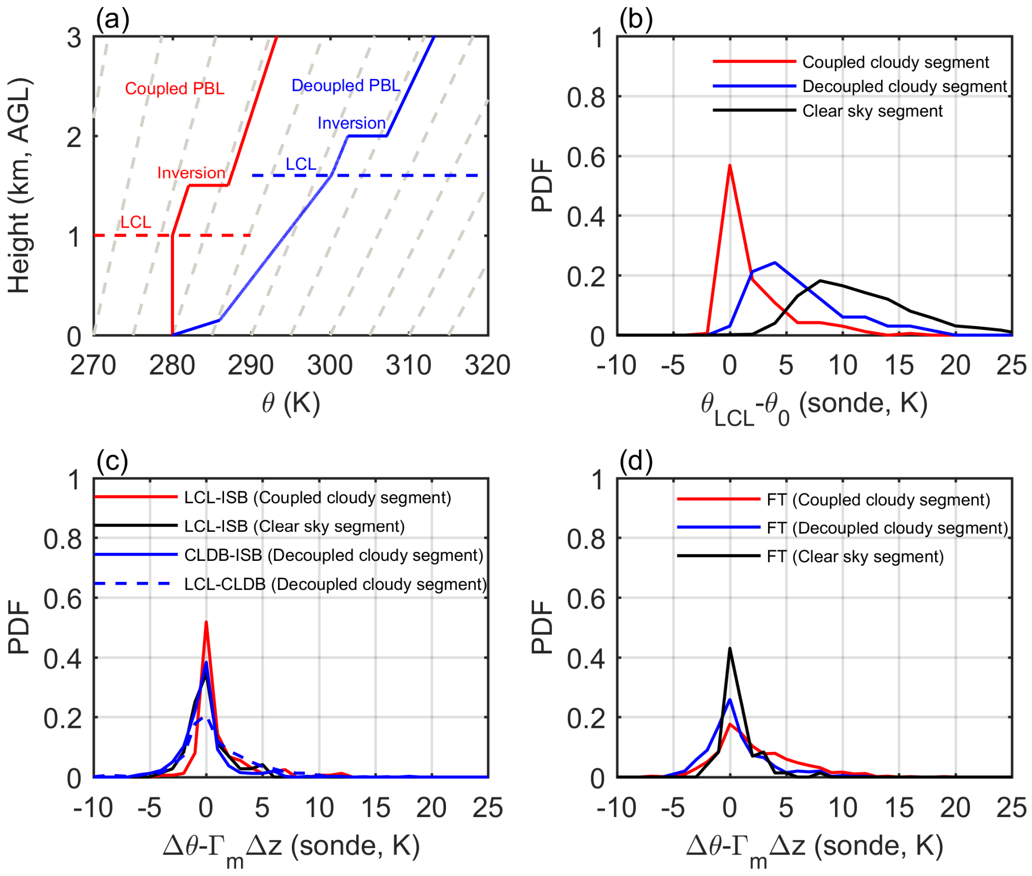

Figure ~~1~~2. Illustrations of PBL θ profiles (a), with the LCL heights indicated by horizontal dash lines and the moist adiabat represented by light dash lines. PDFs of the θ difference between the LCL and 150m AGL (b), the θ difference with the moist adiabat removed between the LCL and the inversion base (c) and the θ difference with the moist adiabat removed for the free troposphere between the inversion top and 3km AGL (d). The red, blue and black lines are for coupled cloudy, decoupled cloudy and clear sky segments, respectively. In (c), the θ differences of decoupled cloudy segments are further separated into that between the LCL and the cloud base (blue dash line) and that between the cloud base and the inversion base (blue solid line).

The characteristics of PBL thermal structures are examined by using the SGP high-resolution radiosondes as shown in Fig.2. Fig. ~~1a~~ 2a illustrates an idealized θ profile ~~for~~ of the ~~coupled~~ well-mixed ~~PBLs~~ condition consistent with ~~that of well-mixed conditions in~~ Wood and Bretherton (2006) and an idealized θ profile ~~for~~ of the decoupled PBLs based on the observations in Jones et al. (2011). The primary difference in the θ profiles between the coupled and decoupled PBLs is whether a stable layer exists to decouple the cloud and subcloud layers (Nicholls, 1984). Hence, under the decoupled conditions, the LTS and EIS ~~could compute~~would include the sum of the PBL IS and the θ increase from the ground to the LCL (the blue line in Fig. 2~~1~~a)~~ as the IS estimates~~. ~~In general, t~~The LTS and EIS can be separated into different terms:

$$\mathrm{LTS} = (\theta_{LCL} - \theta_0) + \Delta\theta + \mathrm{IS}, \qquad (\cancel{8a}9a)$$

$$\mathrm{EIS} = (\theta_{LCL} - \theta_0) + (\Delta\theta - \Gamma_m \Delta z) + \mathrm{IS},$$ (~~8b~~9b)

$$\Delta\theta = \theta_{3km} - \theta_{LCL} - \mathrm{IS},$$ (~~8c~~9c)

$$\Delta z = z_{3km} - z_{LCL}.$$ (~~8d~~9d)

The subscripts of “3km”, “0” and “LCL” indicate the levels of 3km, 150m AGL and LCL. If over oceans, the levels of 3km and 150m can be replaced with 700hPa and 1000hPa. In Eq. (~~8a~~9a), the LTS can be regarded as the sum of the θ difference between the LCL and 150m AGL ($\theta_{\mathrm{LCL}} - \theta_0$), the θ increase ($\Delta\theta$) due to the actual θ gradient above the LCL, and the PBL IS. Similarly in Eq. (~~8b~~9b), the EIS is similar to the LTS except that the θ increase due to the moist-adiabat ($\Gamma_{\mathrm{m}}\Delta \mathrm{z}$) above the LCL is removed. It can be seen that the first two terms on the rhs of Eqs. (~~8a~~9a) and (~~8b~~9b) are contributing to the LTS and EIS even though they are not a part of the IS. In the well-mixed PBLs, the two terms $\theta_{LCL} - \theta_0$ and $\Delta\theta - \Gamma_m\Delta z$ are both equal to zero. Thus the EIS defined as Eq. (~~8b~~9b) is exactly the IS and the LTS defined as Eq. (~~8a~~9a) equals to IS + $\Gamma_m\Delta z$ under perfectly well-mixed conditions.

~~A straightforward indicator to distinguish coupled and decoupled PBLs is the height difference (Δz) between the cloud base and the LCL. An empirical threshold of Δz is 150 meters corresponding to 0.5K of the θ difference in the subcloud layer (Jones et al., 2011). At the SGP, a similar threshold of Δz equal to 180 meters is set to correspond to 0.5K of the θ difference between the cloud base and the LCL. The coupled/decoupled cloudy segments can be directly distinguished by Δz less/greater than 180 meters.~~ At the SGP site, 29%, 32% and 39% observational samples are classified into the coupled cloudy, decoupled cloudy and clear sky segments, respectively. Note that the Δz method cannot distinguish whether the PBL is coupled or decoupled when a segment has no low cloud. Thus the clear sky segments might contain both coupled or decoupled PBL. In Fig. ~~1b~~2b: a) the probability distribution functions (PDFs) of $\theta_{LCL} - \theta_0$ for the coupled cloudy segments peak at zero and ~~have~~ relatively have ~~large~~ positive skewness. The exact reason of the positive skewness is not clear. Because the height of LCL being close to the simultaneously observed cloud base height is only a necessary condition of a PBL being coupled. A decoupled surface layer and overlaying cloud layer coincidently have the height of LCL close to the cloud base is not a surprise. Either clouds advected from other places or a new surface stable layer has developed while clouds formed earlier are still left above might result in positive $\theta_{LCL} - \theta_0$.~~;~~ b) strong stratification below the LCL (large positive $\theta_{LCL} - \theta_0$) frequently occurs in the decoupled cloudy and clear sky segments with mean ~~strength~~ value of 6.3K and 11.5K, respectively. Thus the non-zero term of $\theta_{LCL} - \theta_0$ will cause LTS and EIS to largely deviate from the real value of IS in the decoupled cloudy and clear sky segments.~~Thus the largely positively biased term $\theta_{LCL} - \theta_0$ would be mistakenly counted into the LTS and EIS in the decoupled cloudy and clear sky segments.~~

Besides, a premise of using LTS and EIS to measure the IS ~~even in the coupled PBLs~~ is that the lower-tropospheric θ gradient can be predicted by the moist adiabat above the LCL. This moist adiabatic assumption is supported in previous studies but still with some uncertainties on the daily time scales (Stone, 1972; Wood and Bretherton, 2006; Schneider and O’gorman, 2008). According to PDFs of the θ difference between the LCL and inversion base or between the inversion top and 3km AGL with the moist adiabat removed ($\Delta\theta - \Gamma_m\Delta z$)~~above the LCL~~, θ likely follows the moist adiabat above the LCL (Figs. ~~1c~~ 2c and ~~1d~~2d) with a peak at zero but all PDFs of $\Delta\theta - \Gamma_m\Delta z$ have broad distributions. The standard deviation of $\Delta\theta - \Gamma_m\Delta z$ above the LCL is about 4K. Note that here the Γ_m is computed using the Eq. (5) but based on the temperature and pressure at the base level of each layer.

Typically, the real IS is less than 10K. Thus the term $\theta_{LCL} - \theta_0$ in Eqs. (9a) and (9b) will cause a strong overestimate of the IS by the LTS and EIS. And the variation of the LTS and EIS is attributed to not just variations of IS but also variations of the systematical deviations of temperature profiles from the dry adiabat below the LCL.~~Thus the term $\theta_{LCL} - \theta_0$ due to the systematic deviations of temperature profiles from the dry adiabat below the LCL could easily overwhelm the real IS in Eqs. (8a) and (8b).~~ As a result, at the SGP site, the decoupled cloudy and clear-sky segments (with weak IS but large $\theta_{LCL} - \theta_0$) are ~~largely~~ mixed with the coupled cloudy segments with strong IS when using the LTS and EIS to sort data. Large values of LTS and EIS ~~may~~ correspond to not just strong IS but also weak IS with strong stratification below the LCL. On short time scales (like the daily scale), the spread of $\Delta\theta - \Gamma_m \Delta z$ (Figs. ~~1c~~ 2c and ~~1d~~2d) resulting from the θ gradient deviating from the moist adiabat above the LCL could add additional uncertainty into the LTS/EIS. Hence, weak and even unphysical ~~or weaker~~ relationships ~~between~~ of clouds and ~~/~~moisture ~~and~~ with the LTS/EIS might exist.

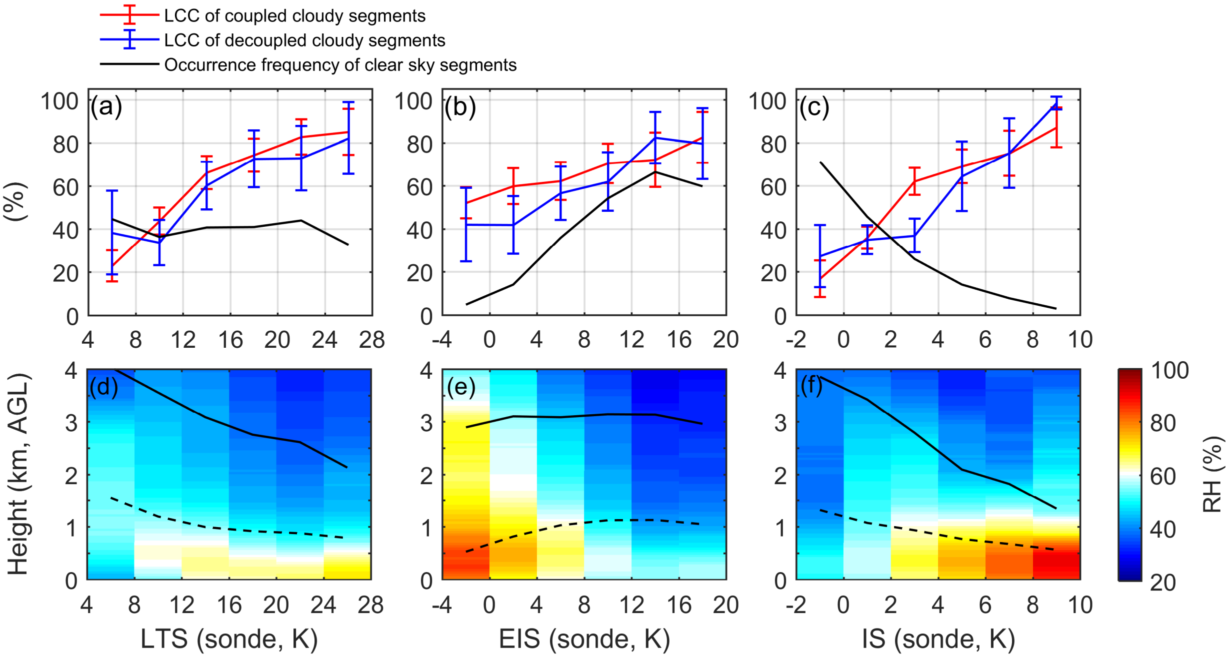

Figure ~~2~~3. Top panel: LCC composites of the coupled cloudy (red line) and decoupled cloudy segments (blue line) and the occurrence frequency of the clear sky segments (black line). Bottom panel: composited RH profiles. Composites are based on the SGP radiosonde-measured LTS (a and d), EIS (b and e) and IS (c and f), respectively. Error bars in (a), (b) and (c) show the 95% confidence interval of the mean based on the t-test. The solid and dash black lines in (d), (e) and (f) indicate the average height of the inversion center and the LCL, respectively. All composites are based on daily data of all seasons for the full period at the SGP.~~All composites are based on daily data.~~

Figs. ~~2a~~3a-c show that the composited LCC of cloudy segments are all positively proportional to the radiosonde-measured LTS, EIS and IS. However, the composites of LCC are slightly/significantly ~~much~~ more sensitive to the changes of IS than the ~~other two estimated metrics~~LTS/EIS. The occurrence frequency of the clear sky segments (the number of clear-sky segments divided by the number of total segments) is investigated separately. ~~Meteorological conditions associated with these hourly segments of no clouds likely extremely disfavor the low cloud formation.~~ Fig. ~~2c~~ 3c shows that clear sky segments are rarely observed when the IS is very strong (~0% at 10K), and more frequently exist towards weaker IS (60% at 0K). This is consistent with that stronger IS inhibits the entrainment of dry air from the free troposphere and thus favors the formation~~/~~ and maintenance of low clouds and corresponds to less occurrence of the clear sky. On the contrary, such a physically reasonable expectation is not seen (even qualitatively) in the composites of the clear sky segments based on the LTS and EIS. Figs. ~~2a~~3a-b show that the occurrence frequency of clear sky segments changes little (even increases) with increasing LTS (EIS). This is also expected based on Fig. ~~1b~~ 2b showing the existence of a large positive skewness in the term $\theta_{LCL} - \theta_0$ in the clear sky segments. This strong static stability below the LCL results in large LTS and EIS even when the real IS is weak.

Composited moisture distribution shows consistent information with the LCC composites. Fig. ~~2f~~ 3f shows that the composited RH has an increasing trend towards stronger IS and high values of RH (RH>80%) are restricted below 1km AGL at the large IS value bins. However, the composited RH distribution is completely reversed when sorted by the EIS, with high/low RH related to weak/strong EIS (Fig. ~~2d~~3d). The RH distribution sorted by the LTS has similar dependence on the magnitude of the LTS (Fig. ~~2c~~3c) to ~~that on~~ the IS, but with weaker variations and smaller PBL RH as compared to the composites based on the IS (Fig. ~~2e~~3e). Thus the LTS/EIS poorly/incorrectly represents the IS at the SGP site, and hence the dependence of the PBL moisture conditions and LCC on the IS are weakly/~~wrongly~~ erroneously reproduced by the LTS/EIS.

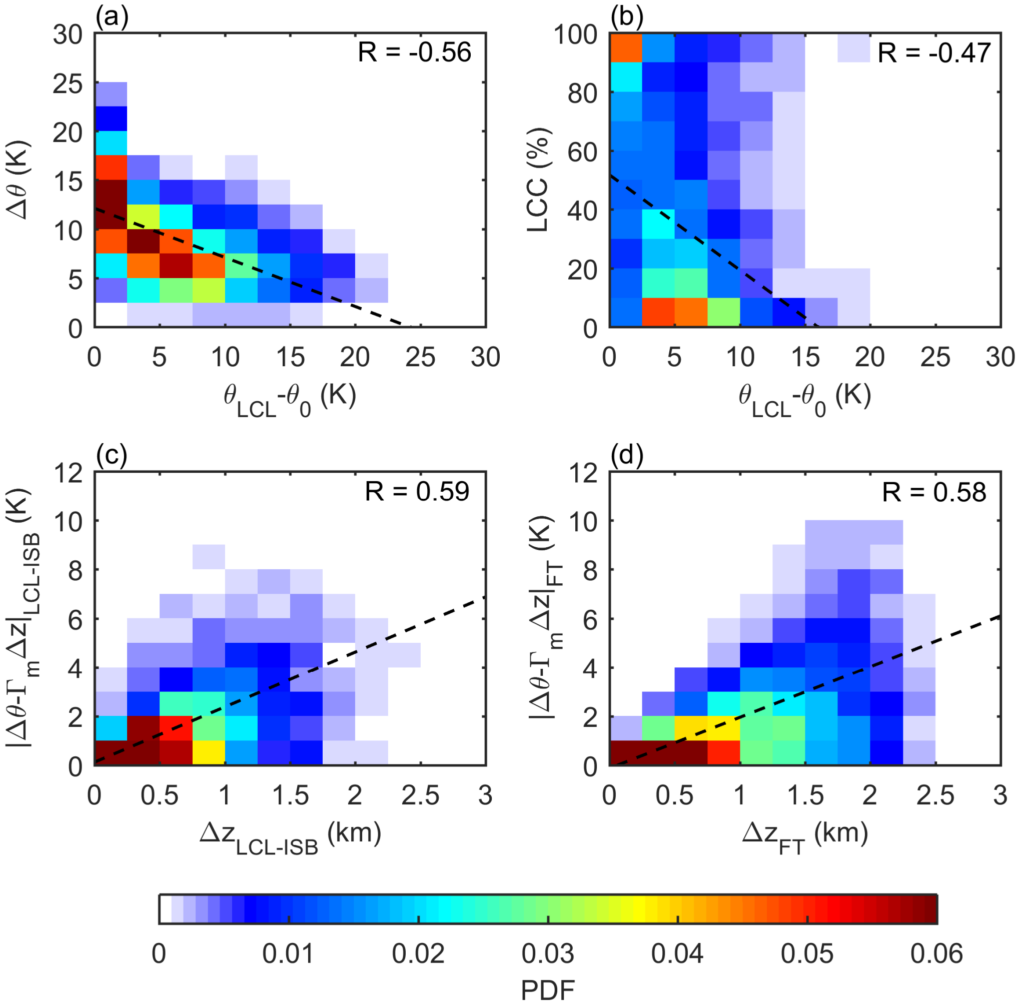

Figure ~~3~~4. Joint PDFs of the θ difference ($\Delta\theta$) between the levels of 3km and the LCL (with the IS excluded) and $\theta_{LCL}-\theta_0$ (a), and PDFs of LCC and $\theta_{LCL}-\theta_0$ (b). Joint PDFs of the absolute value of the θ difference with the moist adiabat removed ($\Delta\theta-\Gamma_m\Delta z$) and the height difference (Δz) from the LCL to the inversion base (c) and from the inversion top to 3km in the free troposphere (d). Correlation coefficients (R) are listed on the upper-right corner of each panel. The black dash lines indicate the least-squares fit.

An interesting phenomenon is that the LTS overall performs better than the EIS with respect to constraining LCC at the SGP site. To understand why this happens, the LTS and EIS in Eq. (~~8~~9) both have been separated into three terms to discuss. For the LTS, the two terms $\theta_{LCL}-\theta_0$ and $\Delta\theta$ of Eq. (~~8a~~9a) usually offset each other with a negative correlation of -0.56 and a slope of the least-squares fit -0.5K/K (Fig. ~~3a~~4a). In contrast, the slope of the least-squares fit between $\Delta\theta-\Gamma_m\Delta z$ and $\theta_{LCL}-\theta_0$ is only -0.05K/K (not shown). ~~Thus~~Furthermore, the LTS and EIS equation can be transformed into:

LTS ~~≈~~ $= \left(1+\frac{\Delta\theta}{\theta_{LCL}-\theta_0}\right)(\theta_{LCL}-\theta_0)+\mathrm{IS}.$ (~~9~~10a)

EIS $= \left(1+\frac{\Delta\theta-\Gamma_m\Delta z}{\theta_{LCL}-\theta_0}\right)(\theta_{LCL}-\theta_0)+\mathrm{IS}.$ (10b)

On average, the coefficient before $\theta_{LCL}-\theta_0$ for the LTS in Eq. (10a) is 0.5 while that for EIS in Eq. (10b) is 0.95. The variation of LTS and EIS result from both the changes of IS (positively correlated with LCC as shown in Fig. 3c) and the changes of $\theta_{LCL}-\theta_0$ (negatively correlated with LCC as shown in Fig. 4b). According to Eqs. (10a) and (10b), the LTS actually only involves half of the bias caused by $\theta_{LCL}-\theta_0$ and thus not as strongly influenced by $\theta_{LCL}-\theta_0$ as the EIS. As a result, only removing the moist adiabat ($\Gamma_m\Delta z$) does not make the EIS a better estimate for the IS at the SGP but make the EIS more influenced by $\theta_{LCL}-\theta_0$. This explains why the LTS is better correlated with LCC and RH (Figs. 3a and 3d) than the EIS (Figs.

3b and 3e) at the SGP. However, the physical reason that why the PBL stratification changes in this way is unclear to us and it is beyond the scope of this study.~~According to the offset of those two terms, the coefficient of $\theta_{LCL} - \theta_0$ in Eq. (9) is ~0.5. This means that the biases added to the LTS is about a half of that for the EIS defined as Eq. (8b). Fig. 3b shows that the term $\theta_{LCL} - \theta_0$ is negatively correlated (a correlation of -0.47) with LCC in contrast to the positive LCC-IS correlation. Thus if large deviations from the dry adiabat below the LCL exist, the LTS actually is a better measure of IS than the EIS, since less biases resulting from the term $\theta_{LCL} - \theta_0$ are involved in the computation of LTS. As shown in Fig. 2, the LTS has positive but relatively weak correlations with the LCC and RH, but the EIS is negatively correlated with them.~~

As shown in Figs. ~~1c~~ 2c and ~~1d~~2d, the θ difference between the actual environmental θ gradient and the moist adiabatic θ gradient ($\Delta\theta - \Gamma_m \Delta z$) is another source of uncertainty in the EIS based on Eq. (~~8b~~9b), especially on short time scales. However, Figs. ~~3c~~ 4c and ~~3d~~ 4d suggest that the spread of $|\Delta\theta - \Gamma_m \Delta z|$ increases with the layer thickness either between the LCL and the inversion base or between the inversion top and 3km AGL (with a correlation of 0.59 or 0.58, respectively). Thus, the thicker the layer encompassing inversion involved in the EIS calculation is, the larger the uncertainty is. Including more layers around the inversion layer in estimating the IS likely results in more uncertainty. This suggests a possible way of better estimating the IS if we can reduce the layer thickness (Δz) associated with the second term on the rhs of Eq. (9b), which also makes the IS estimate less dependent on the moist adiabatic assumption.~~This is because that the term $\Delta\theta - \Gamma_m \Delta z$ can also be written as $(\Gamma - \Gamma_m)\Delta z$, where Γ is the environmental θ gradient. This suggests a possible way of reducing uncertainties in estimating the IS if we can reduce the layer thickness (Δz) associated with the second term on the rhs of Eq. (8b) when using it to estimate the IS.~~

Above results suggest that there are two major bias and error sources of estimating the IS using the LTS and EIS metrics. One is caused by systematic deviations from the dry adiabat below the LCL, the other is the errors resulting from the spread of the actual θ gradient around the moist adiabat above the LCL. To exclude the former source, we can locate the LCL and only consider the inversion above the LCL to drop the first term on the rhs of Eq. (9b). The impact of the latter one can be indirectly reduced by finding the thinnest layer of encompassing the inversion that is involved in the computation of the second term on the rhs of Eq. (9b). Thus, the new EIS_p (as described in section 3.1) is proposed accordingly to achieve a better estimate of the IS.

~~3.2 The algorithm of the new EIS_p and its relationship with LCC at the SGP~~

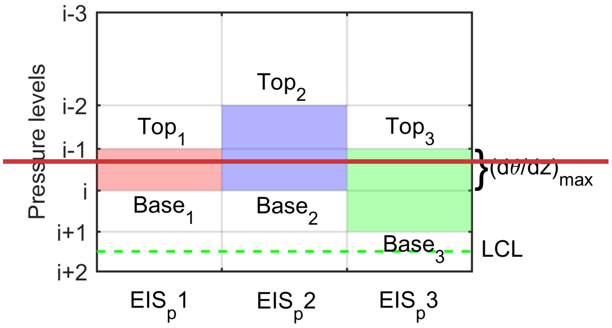

~~Figure 4. An illustration of finding the location of three possible layers encompassing the inversion in one ERA5 profile. The red block refers to one single ERA5 layer. The blue and green each refers to a combination of two adjacent ERA5 layers. Three candidate EIS_ps (EIS_p1-3) are computed accordingly.~~

~~Above results suggest that there are two major bias and error sources of estimating the IS using the LTS and EIS metrics. One is caused by systematic deviations from the dry adiabat below the LCL, the other is the errors resulting from the spread of the actual θ gradient around the moist adiabat above the LCL. To exclude the former source, we can simply locate the LCL to drop the first term on the rhs of Eq. (8b). The impacts of the latter one can be indirectly reduced by reducing the layer~~

~~thickness that is involved in the computation of the second term on the rhs of Eq. (8b). Specifically, we construct a profile-based IS estimate (EIS_p):~~

~~$$EIS_p = (\Delta\theta - \Gamma_m \Delta z) + IS, \quad (10a)$$~~

~~$$\Delta\theta = \theta_{top} - \theta_{base} - IS, \quad (10b)$$~~

~~$$\Delta z = z_{top} - z_{base}, \quad (10c)$$~~

~~where subscripts “top” and “base” represent the top and base levels for computing the EIS_p. Instead of using the two fixed levels in the LTS and EIS, the top and base levels of the inversion layer in the EIS_p are determined by scanning the ERA5 profiles above the LCL. Fig. 4 illustrates how to find the top and base levels of three possible layers encompassing the inversion. One possible layer is the layer corresponding to the maximum $d\theta/dz$ (red zone). Other two possible layers are the blue and green zone referring to the combination of the layer of maximum $d\theta/dz$ and the layer just above or below it, respectively. After finding the targeted layers, three candidate EIS_ps are computed using Eq. (10) and the largest one among three is selected as the EIS_p.~~

~~By this method, the term $\theta_{LCL} - \theta_0$ in the LTS and EIS is completely removed in the EIS_p. The term $\Delta\theta - \Gamma_m \Delta z$ in the EIS is reduced according to Figs. 3c and 3d, since the thickness of the layer involved in the computation of the LTS/EIS (from the LCL to 3km) is reduced to about 0.3~1km in the EIS_p. This method is suitable for the PBLs with a dominant inversion when used with the ERA5 reanalysis. If multiple inversions with comparable strength occur, this method may not always find the strongest inversion especially if the strongest inversion is distributed into two reanalysis layers. Because this method is designed to find the inversion above the LCL and this height constraint directly filters out the possible large stability below the LCL (e.g., surface-based inversion or decoupled layers), the occurrence of strong secondary inversions is likely rare.~~

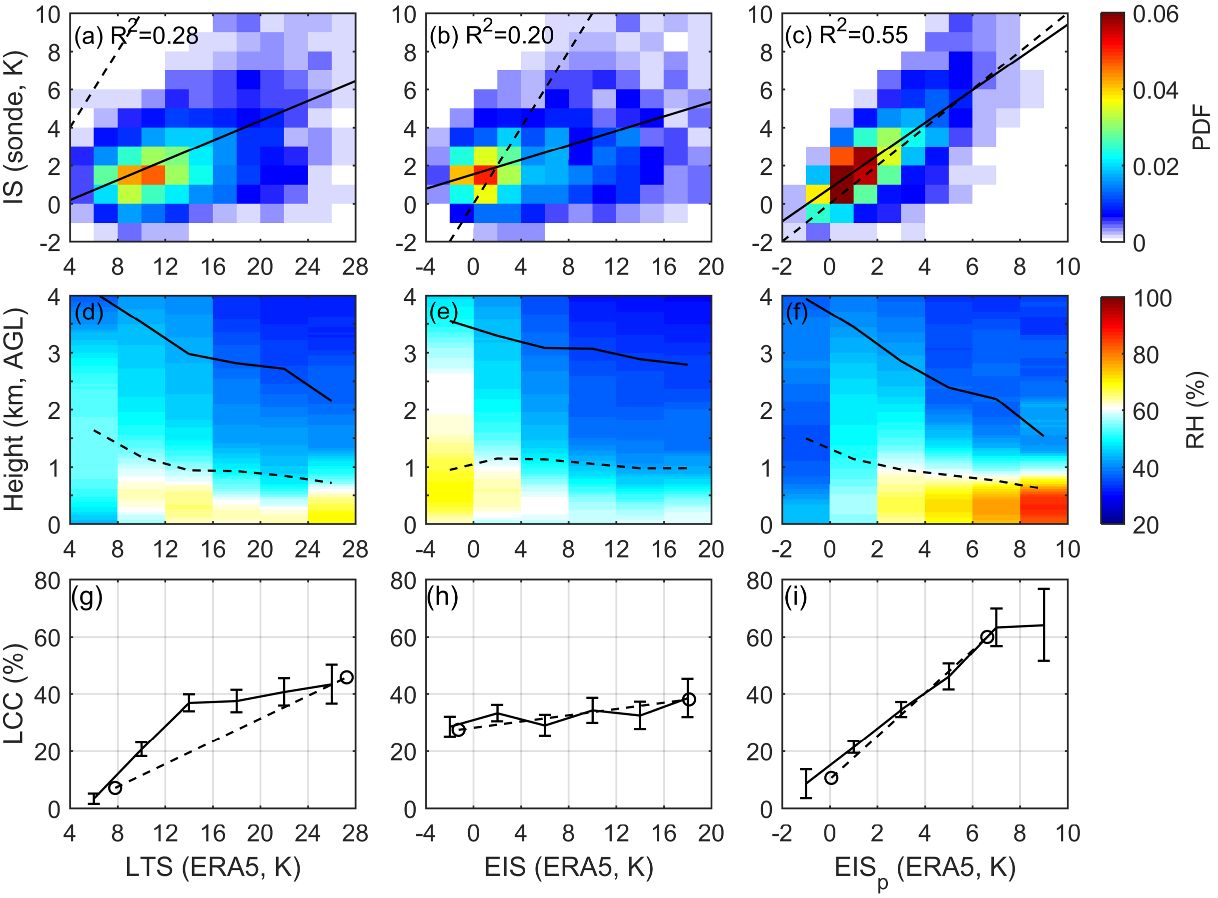

Figure 5. Joint PDFs of the SGP radiosonde-measured IS, and the ERA5-derived LTS (a), EIS (b) and EIS_p (c), respectively. In (a)-(c), the black solid line is the least-squares fit and the dash line is the reference line of y=x. The composites of the radiosonde RH profiles based on the ERA5-derived LTS (d), EIS (e) and EIS_p (f). The black solid and dash lines in (d-f) are the heights of the IS and the LCL, respectively. The LCC composited based on the LTS, EIS and EIS_p are shown in (g), (h) and (i), respectively. The cycles in (g), (h) and (i) corresponds to the 5% and 95% quantile of LTS, EIS and EIS_p and the

composited value of LCC in the bins of the smallest and largest 10% of LTS, EIS and EIS$_p$ values. Error bars in (g-i) show the 95% confidence interval of the mean based on the t-test.

The LTS, EIS and EIS$_p$ derived from the hourly ERA5 reanalysis are directly compared against the SGP radiosonde-measured IS. In Fig. 5c, the R-square between the EIS$_p$ estimated from the ERA5 and the IS measured by radiosondes is 0.55, which is much larger than that of the LTS (0.28, Fig. 5a) and EIS (0.20, Fig. 5b). The slope of the least-squares fit of the IS to the EIS$_p$ is 0.86K/K. This indicates the ~~range~~ value of the EIS$_p$ is much closer to ~~that of~~ the IS as compared to ~~that of~~ the LTS (0.26K/K) and EIS (0.19K/K). The composites of LCC and RH based on the EIS$_p$ (Fig. 5f) show similar results to that based on the IS (Fig. ~~2f~~3f). Stronger EIS$_p$ corresponds to larger RH trapped below about 1km, ~~while~~ and with the EIS$_p$ weakening and the inversion layer lifting RH decreases but distributes to higher levels~~decreasing RH (but penetrating to higher levels) with weakening and lifting inversion layers~~. However, the LCC and RH composites based on the LTS and EIS (Figs. 5d, 5e, 5g and 5h) show weak or ~~wrong~~ erroneous relationships similar to the results based on the radiosonde-measured LTS and EIS (Fig. ~~2a~~3a, ~~2b~~3b, ~~2d~~ 3d and ~~2e~~3e). Thus the EIS$_p$ ~~does a better job on estimating the~~offers a better fit to the real IS and better constrains the PBL moisture distribution and LCC. The slope of the composited LCC to the EIS$_p$ is 6%/K, in contrast to that to the LTS (1.9%/K) and the EIS (0.4%/K). Since the range of the LTS and EIS is larger than that of the EIS$_p$, larger slopes of the LCC to the EIS$_p$ than that to the LTS and EIS are expected. To measure the sensitivity of LCC to changes of LTS, EIS and EIS$_p$, we consider the effective range of LCC resolved by changes in a metric. The sensitivity of LCC to a metric here is defined as the difference between the composited LCC values associated with the largest and smallest 10% of that metric:

$$LCC\ Sensitivity\ to\ x = \overline{LCC(x \geq x_{90\%})} - \overline{LCC(x \leq x_{10\%})}. \qquad (11)$$

The bar over the LCC head represents the mean value of LCC sorted by x quantile. $x_{90\%}$ and $x_{10\%}$ are 90% and 10% quantile of x. The LCC sensitivity of all segments to the EIS$_p$ is 50%, which is larger than the LTS (39%) and EIS (12%). These weaker/erroneous dependences of LCC on the LTS/EIS are expected since large errors (Figs. ~~1b~~2b-~~1d~~2d) are carried in ~~when the IS is estimated by~~ the LTS/EIS. Although the ~~relatively lower~~ vertical resolution of the ERA5 profiles may not always suffice to resolve the inversion layer, the IS estimated from the ERA5 profile-based algorithm (EIS$_p$) is highly consistent with the IS directly derived from the SGP 10m-resolution radiosondes and they present similar relationships with the PBL RH and LCC.

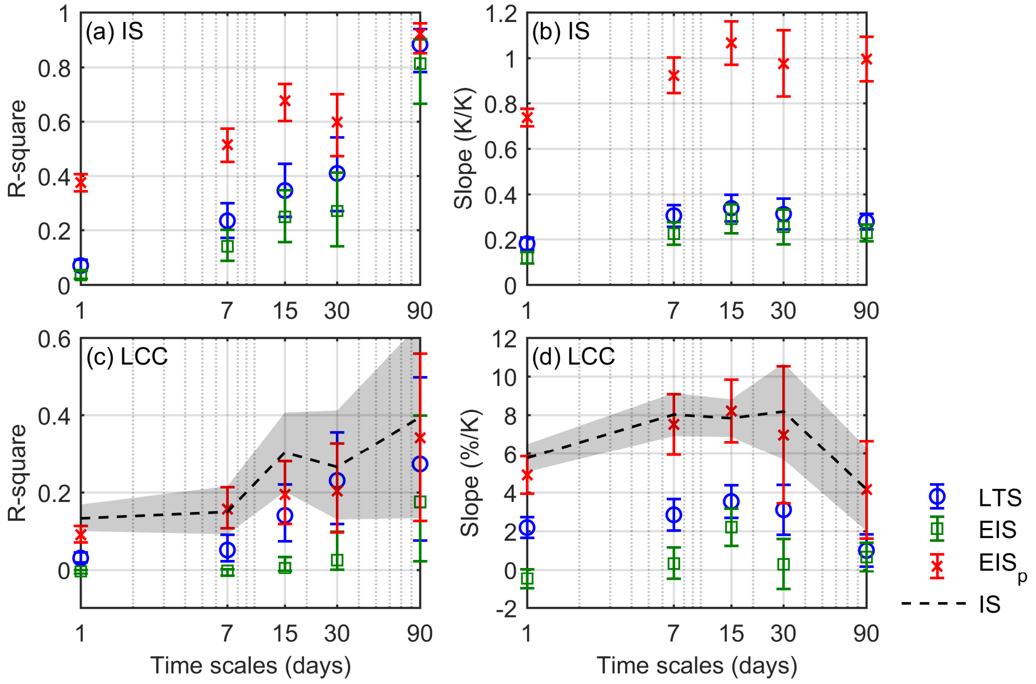

Figure 6. R-square (a) and slope of the least-squares fit (b) of the SGP radiosonde-derived IS to the ERA5 reanalysis-based LTS (blue cycle), EIS (green square) and EIS$_p$ (red cross) on daily, 7-day, 15-day, 30-day and 90-day time scales, respectively.

R-square (c) and slope (d) of LCC to the LTS, EIS, EIS$_p$ and IS (black dash line) on daily to seasonal time scales, respectively. Error bars and shadows show the 95% confidence interval of the mean based on the t-test.

The ERA5-based LTS, EIS and EIS$_p$ are further examined on the different time scales with respect to their relationships with radiosonde-measured IS and LCC (Fig. 6). Overall, the R-square and the slope ~~between~~ of the EIS$_p$ ~~and~~ with the IS are the largest through all time scales as compared to that of the LTS and EIS. Particularly on the daily, 7-day and 15-day time scales, the lower bounds of the 95% confidence interval of the EIS$_p$-IS R-square are much higher than the upper bounds for the LTS and EIS. On the seasonal time scale, three metrics have similar correlations with the IS, but as shown in Fig. 6b, the slope of the IS to the EIS$_p$ (nearly 1) is still much larger than that to the LTS (0.28K/K) and EIS (0.23K/K). The limited accuracy restricts the LTS and EIS to reproduce the relationship between the true IS and LCC. In Fig. 6c, on daily time scales, the LTS explains 3.1% of variance in LCC, which is comparable to the 4.8% explained variance by the LTS at OWS N (a typical low-cloud dominated site over the ocean) in Klein (1997). For the EIS$_p$, it explains 9.1% of the daily LCC variance, which is remarkably close ~~not bad as compared~~ to that explained by the IS ~~(12-13%)~~. Similar conclusions can be drawn from weekly time scales. On longer time scales, the EIS$_p$ and the LTS both explain comparable variance in LCC but much larger than that explained by the EIS. In Fig. 6d, the slope of LCC composited based on the IS is nearly reproduced by the EIS$_p$ consistently. The slopes of LCC composited based on the LTS and EIS are much smaller than that based on the EIS$_p$ and IS.

~~4. Evaluation of the LTS, EIS and EIS$_p$ at the global scale~~

~~4.1~~3.3 Validation of the EIS$_p$ at radiosonde stations of subtropics and midlatitude ~~At worldwide radiosonde stations~~

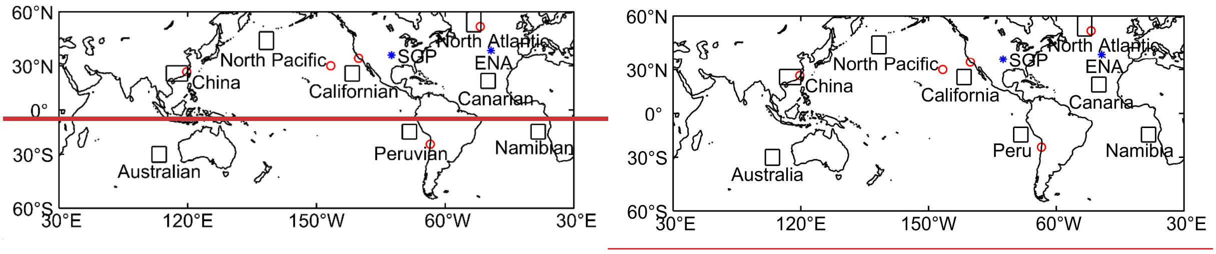

Figure 7. Blue asterisk marks the SGP and ENA sites. Red cycles mark the locations of radiosonde stations from the IGRA. Eight 10°×10° boxes are the most typical low-cloud dominated regions defined in Klein and Hartmann (1993).

Table 2. The characterestics of the PBL thermal strucures, evaluation of the LTS, EIS and EIS$_p$ on estimating the IS and the IS-LCC relationships of the six radiosonde stations. Coupled and decoupled PBLs of all stations are distinguished by α_θ. Italic indicates not significant correlations. Italic indicates not significant correlations. Bold indicates the largest correlation. The daily IS-LCC correlation is based on the data after subtracting 7-day means~~dataset excluding 7-day means~~.

	ARM SGP	ARM ENA	OWS N	OWS C	Tropical East Pacific Coast	Southeast Pacific Coast	Chinese Coast
θ_{LCL}-θ_0 in coupled PBLs (standard deviation)	0.33K (0.36K)	0.26K (0.39K)	1.33K (0.74K)	0.85K (0.86K)	0.70K (1.34K)	0.17K (0.28K)	0.16K (0.93K)
θ_{LCL}-θ_0 in decoupled PBLs (standard deviation)	8.69K (5.82K)	2.55K (2.37K)	3.53K (2.23K)	2.73K (2.30K)	10.46K (6.71K)	1.41K (2.05K)	3.34K (3.50K)
$\Delta\theta - \Gamma_m \Delta z$ above the LCL (standard deviation)	1.22K (3.98K)	0.07K (1.64K)	-0.39K (2.26K)	1.65K (2.74K)	-1.06K (2.36K)	0.48K (2.34K)	-1.16K (2.93K)
IS-LTS correlation	0.53	0.51	0.35	0.29	0.43	0.62	0.62
IS-EIS correlation	0.45	0.58	0.41	0.36	*-0.06*	0.53	0.76
IS-EIS$_p$ correlation	**0.74**	**0.76**	**0.60**	**0.48**	**0.75**	**0.74**	**0.79**
IS-LCC daily correlation (slope ± confidence intervals)	0.34 (2.82 ± 0.42%/K)	0.16 (3.05 ± 0.97%/K)	NAN	NAN	0.26 (2.61 ± 0.43%/K)	0.30 (2.71 ± 0.39%/K)	0.16 (3.07 ± 0.85%/K)
IS-LCC monthly	0.65 (3.65 ±	0.43 (6.44	NAN	NAN	0.38 (6.95 ±	0.71 (4.52 ±	0.76 (6.57 ±

correlation (slope ± confidence intervals)	0.78%/K)	± 3.34%/K)		4.02%/K)	1.06%/K)	1.38%/)

As shown in section 3.2, at the ARM SGP site, the EIS$_p$ better estimates the PBL IS~~does work better~~ than both the LTS and EIS ~~on estimating the PBL IS~~ when the PBL thermal structure is largely deviated from the idealized structure of well-mixed PBLs. Next, we want to see if such a deviation exists at other radiosonde stations of subtropics and midaltitude~~globally~~. The ARM ENA site and other five ground-based radiosonde stations are selected to examine their characterestics of PBL thermal strucures. Their locations are shown in Fig. 7. Because the cloud base height information is not available at the radiosonde stations of IGRA, the method used at the SGP to distinguish the coupled-cloudy, decoupled-cloudy and clear sky segments is not accessible. Thus, an alternative indicator, the decoupling degree (α_θ), is used to distinguish coupled and decoupled PBL according to the PBL thermal structures. The definition of α_θ is introduced in Wood and Bretherton (2004) by using the liquid potential temperature (θ_L) as the conserved variable during the moist adiabat. Here, θ is used to construct the moist-adiabatic conserved variable by removing the moist-adiabatic θ increase above the LCL to express the α_θ parameter:~~, the coupled and decoupled PBLs now are determined by the α_θ:~~

$$\alpha_\theta = \frac{\theta_{ISB}-\theta_0-\Gamma_m(z_{ISB}-z_{LCL})}{\theta_{IST}-\theta_0-\Gamma_m(z_{IST}-z_{LCL})} \cancel{= \frac{\theta_{LCL}-\theta_0+[\theta_{ISB}-\theta_{LCL}-\Gamma_m(z_{ISB}-z_{LCL})]}{IS+\theta_{LCL}-\theta_0+[\theta_{ISB}-\theta_{LCL}-\Gamma_m(z_{ISB}-z_{LCL})]}}. \tag{12}$$

The subscripts “ISB”, “IST”, “0”, “700hPa” and “LCL” indicate the base and top of inversion layers, the ~~1000hPa~~ levels of 1000hPa and 700hPa and the LCL, respectively. To understand its meaning, Eq. (12) can be transformed as:

$$\alpha_\theta = \frac{\theta_{LCL}-\theta_0+[\theta_{ISB}-\theta_{LCL}-\Gamma_m(z_{ISB}-z_{LCL})]}{IS+\theta_{LCL}-\theta_0+[\theta_{ISB}-\theta_{LCL}-\Gamma_m(z_{ISB}-z_{LCL})]} \approx \frac{EIS-IS}{EIS}. \tag{13}$$

The numerator of α_θ can be understood as the strength of the PBL thermal structures deviating from the coupled conditions. The denominator of α_θ can be understood as the sum of the deviation strength of the PBL thermal structure from the coupled conditions and the IS (or EIS). By Eq. (13), the EIS can also be expressed as $IS/(1-\alpha_\theta)$. Thus, whether the EIS is the real IS is actually determined by the decoupling parameter α_θ. In perfectly coupled conditions, α_θ is zero and the EIS is exactly the IS. In decoupled PBLs, when α_θ is larger, the EIS actually more accounts for the deviation of the PBL thermal structure from the coupled condition. A small value of α_θ would suggest a state very close to the coupled condition and here a threshold value of 0.2 is used to distinguish the coupled/decoupled PBLs based on Eq. (12). ~~α_θ expresses the decoupling degree and is similar to that defined in Wood and Bretherton (2004), by removing the moist-adiabatic θ increase above the LCL. In perfectly coupled conditions, the numerator of Eq. (12) should be zero. Otherwise, the decoupling degree is in proportion to α_θ. In the tropical and subtropical well-mixed regions, the median value of α_θ is usually less than about 0.2 (Wood and Bretherton, 2004) and thus a threshold of α_θ here is set as 0.2 to distinguish the coupled/decoupled PBLs.~~ α_θ has been tested for the high-resolution soundings and it comes to similar results. In fact, results listed in Table 2 at the SGP based on α_θ show consistent results with that based on Δz_b.

As shown in Table 2, it is found that the two terms $\theta_{LCL}-\theta_0$ and $\Delta\theta-\Gamma_m\Delta z$ in Eq. (~~8~~9) are non-negligible even over the subtropical oceans. Both the mean and standard deviation of $\theta_{LCL}-\theta_0$ are very small in the coupled PBLs. The mean of $\theta_{LCL}-\theta_0$ at the other sites in the decoupled PBLs is usually smaller (about 1-4K) as compared to that at the SGP (8.69K), except at the tropical east Pacific coast, which is larger (10.46K) than that at the SGP. Theoretically, a constant shift on the θ difference between the LCL and the ground level will not change the correlation coefficient and regression slope between the LTS/EIS and the IS/LCC. However, the term $\theta_{LCL}-\theta_0$ is systematically different between the coupled and decoupled PBLs. Thus using the LTS and EIS to sort the PBL structures will unequally mix the coupled and decoupled conditions in their different composite bins. Moreover, this bias is distinct for different places and thus the regional difference would make the LTS and EIS not uniform for their accuracies of estimating the IS. In contrast, this will not happen in the EIS$_p$ since this bias caused by the term $\theta_{LCL}-\theta_0$ in the LTS and EIS is completely excluded from the EIS$_p$.

The standard deviation of the term $\Delta\theta-\Gamma_m\Delta z$ as shown in Table 2 suggests that the errors of estimating the IS based on

Eq. (~~8~~9) due to the moist adiabatic assumption above the LCL of the ENA and other five radiosonde sites range from 57%-74% of that of the SGP site (3.98K). Thus the term $\Delta\theta - \Gamma_m \Delta z$ at these six sites will likely also be reduced when measuring the IS by the EIS$_{p.}$ Thus it is not surprising that the ERA5 EIS$_p$ is best correlated with the IS directly derived from the radiosondes over all stations (Table 2). Regional differences of the correlations with the IS still exist for all metrics to measure the IS but are relatively small for the EIS$_p$.

4.~~.2~~ On the relationship of global LCC with LTS, EIS and EIS$_p$ ~~Relationship between global LCC and LTS, EIS and EIS$_p$~~

In this section, the relationship of global LCC with LTS, EIS and EIS$_p$ is discussed through daily to seasonal time scales. Since ground-based observations of radiosondes from ARM and IGRA are all assimilated in the ERA5 reanalysis (Hersbach et al., 2020), it is not surprising that the assimilated output can well capture the PBL thermal structures to estimate the IS for these locations where ground-based observations are available. However, for most areas of oceans, only limited radiosondes are available over scattered islands or during short-term campaign of field experiments to be used in ERA5 assimilation and thus whether the IS can be right captured from the ERA5 profiles needs further examination. In this section, whether the EIS$_p$ derived from the ERA5 profiles at the global scale (especially for oceans with few radiosondes assimilated into the ERA5) can better constrain LCC than LTS and EIS is explored.

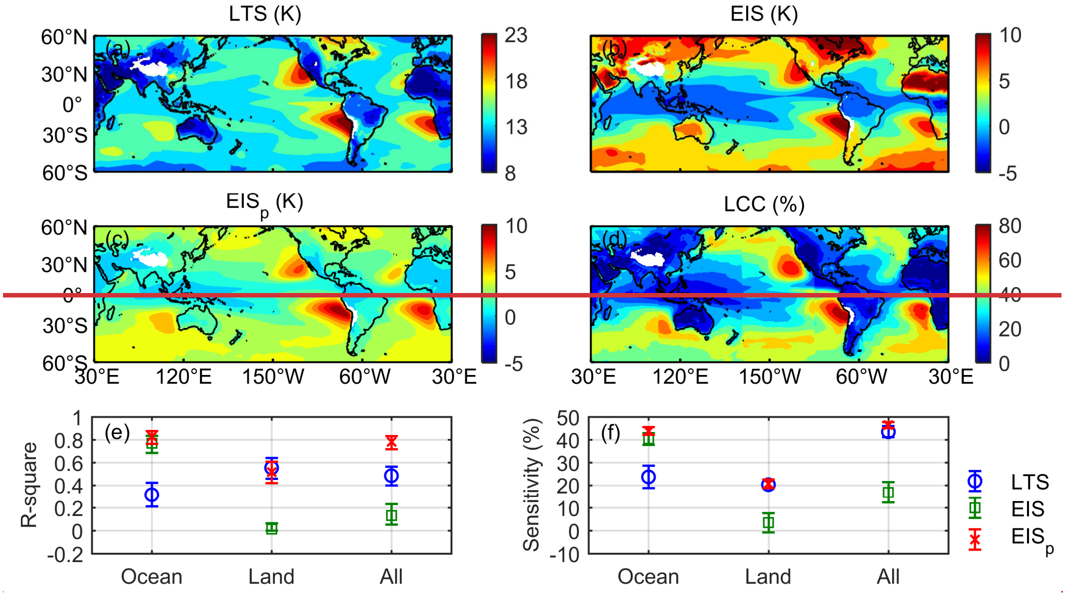

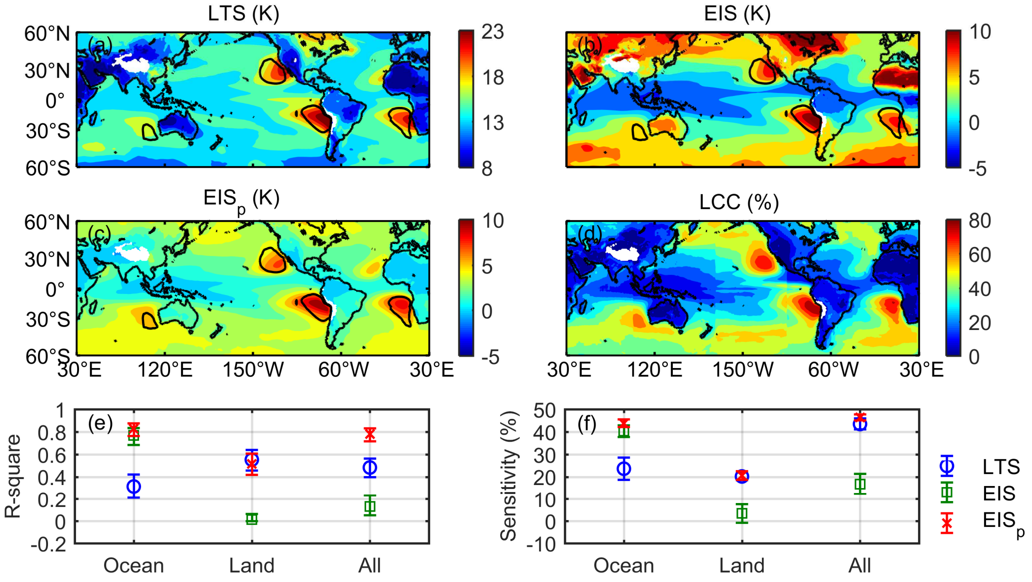

Figure 8. Spatial distribution of the ERA5 reanalysis-based LTS (a), EIS (b), EIS$_p$ (c) and the GEO-MODIS LCC between 60ºS and 60ºN. The black contours enclose regions with LCC larger than 60%. The specific R-square and LCC sensitivity to the LTS (blue cycle), EIS (green square) and EIS$_p$ (red cross) over the ocean, land and all is shown in (e) and (f), respectively. The error bars show the 95% confidence interval of the mean based on the t-test.

Fig. 8 shows the six-year mean map of the ERA5-based LTS, EIS and EIS$_p$. The GEO-MODIS LCC global pattern is also used to examine its spatial correlation with the above three metrics. For the LTS, EIS and EIS$_p$, the plateau regions with the surface pressure smaller than 700hPa are not investigated here, where no GEO-MODIS LCC is observed. Overall, the annual mean value of LTS and EIS are obviously larger than the EIS$_p$ value except the inner tropical convective zone where the EIS value is large negative. In addition, there are three differences between the spatial distributions of LTS, EIS and EIS$_p$.

(1) *Over the subtropical eastern oceans*, the center locations of LTS, EIS and EIS$_p$ are different. For LTS and EIS, their center locations are more eastward and adjacent to the coast as compared with the center locations of EIS$_p$ and LCC. For EIS$_p$, its center locations are relatively away from the coast and more consistent with the center locations of LCC.

(2) *Over midaltitude oceans*, the contrast of the values between the midlatitude and the tropics is different for LTS, EIS and EIS$_p$. The midlatitude LTS reduces to the minimum but still corresponds to about 40% of LCC. The midlatitude EIS is as strong as the EIS over the subtropical eastern oceans but corresponds to the LCC much smaller than the subtropical LCC. Only the variation of EIS$_p$ from tropics to midlatitude is more reasonably consistent with the spatial variation of LCC.

(3) *Over land*, the LTS and EIS$_p$ explains over half of the LCC spatial variance according to their linear fit, but the EIS only explains 2% of the LCC spatial variance. This implies the IS is still a controlling factor for LCC distribution over land. The EIS barely correlates to continental LCC possibly because the EIS poorly estimates IS due to the strong influence of the term $\theta_{LCL} - \theta_0$ as discussed in section 3.

On the whole, the performance of EIS$_p$ is better and less dependent on surface types. Over all global oceans and land, the EIS$_p$ explains 78% of the spatial variance in LCC, significantly higher than that explained by the LTS (48%) and the EIS (13%). The spatial variations of LCC are also more sensitive to the EIS$_p$ (Fig. 8f).

~~Over the ocean, the EIS$_p$ distribution better corresponds to the pattern of LCC and explains 83% of its spatial variance, higher than that explained by the EIS (77%) and the LTS (31%). Particularly, the locations of the five subtropical strongest EIS$_p$ centers over the eastern oceans are relatively away from the coast (Fig. 8c). This is consistent with the locations of corresponding large LCC centers. In contrast, the centers of strong LTS (Fig. 8a) and EIS (Fig. 8b) are usually over the west coasts, slightly shifting away from those centers of LCC, though these places are usually regarded as the most likely well-mixed PBLs. Over the midlatitude ocean, it is also noted that the LTS value is too small to explain large LCC, and the EIS value is comparable to that over the subtropics but corresponds to LCC much less than the subtropical LCC. Compared with~~

~~the LTS and EIS, the distribution of EIS$_p$ over global oceans more reasonably explains the LCC spatial variations. Over land, the EIS$_p$ and LTS distribution still well corresponds to the LCC pattern and explains over half of the LCC spatial variance. This implies the IS is still a possible controlling factor for LCC over land and thus accurately estimating the IS over land is also necessary to explain continental LCC variations. But the EIS over land does a much worse job in most areas and only explains 2% of the spatial variance of LCC. The exact reason of this phenomenon is not known, but seems the poor fault tolerance of the EIS on the term $\theta_{LCL} - \theta_0$ as shown in section 3 might be one reason. The LTS cannot well explain the oceanic spatial LCC variations and the EIS cannot well explain the continental spatial LCC variations. But these will not happen with the EIS$_p$. Over global oceans and land, the EIS$_p$ explains 78% of the spatial variance in LCC, significantly higher than that explained by the LTS (48%) and EIS (13%). The spatial variations of LCC are also more sensitive to the EIS$_p$ (Fig. 8f).~~

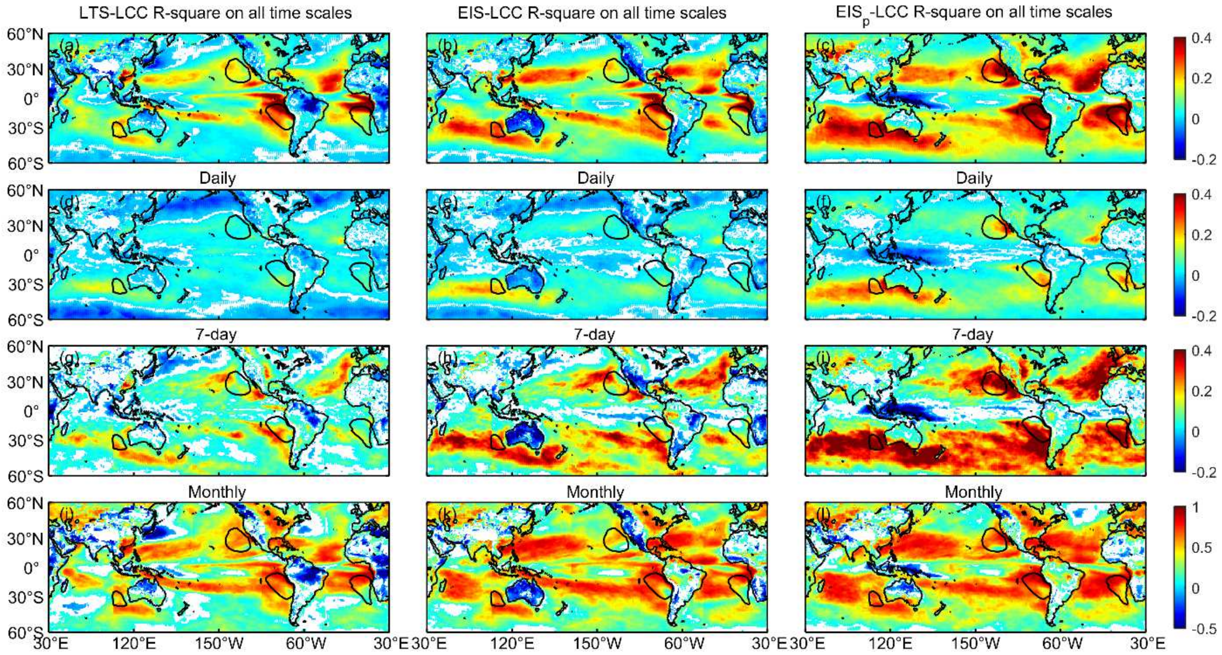

Figure 9. R-square between the GEO-MODIS LCC and the ERA5 reanalysis-based LTS (left column), EIS (middle column) and EIS$_p$ (right column) at the all-time scales (a, b and c), daily time scale (d, e and f), 7-day time scale (g, h and i) and monthly time scale (j, k and l). The black contours enclose regions with LCC larger than 60%. Only correlations at the 95% significant level are shown. The minus/plus sign of R-square indicates negative/positive correlations.

In Fig.9, t~~T~~he dependence of LCC on the ~~three ERA5-based metrics~~LTS, EIS and EIS$_p$ is further examined globally for the full daily time series (i.e., all time scales) and for the daily, 7-day window-averaged anomalies and monthly means (i.e., daily, 7-day and monthly time scales)~~on different time scales~~. It is noted that the dependence of LCC on the three ERA5-based metrics are variant across different regions. LCC is best correlated with three metrics over the subtropical eastern oceans and some land regions that are most dominated by low clouds. Over midlatitude oceans and inner tropical convergence zone, the LCC is weakly or negatively correlated with three metrics. Thus, it is discussed separately for the most LCC-dominated regions over subtropical oceans, midlatitude oceans and land.

(1) *Over the subtropical eastern oceans with more than 60% of LCC*, on all time scales (Figs. 9a-c), the EIS$_p$ explains 36% of the variance in LCC on average, larger than that explained by the LTS (21%) and the EIS (20%). The fact that EIS does not provide a stronger correlation with LCC than LTS was also recognized by Park and Shin (2019) and Cutler et al. (2022). In contrast, the explained variance of the linear fitting between LCC and EIS$_p$ is 1.8 times of that with LTS and EIS. Besides, the mean LCC sensitivity (defined in Eq. (11) and not shown in the figure) to the EIS$_p$ on all time scales is 48% over these regions, significantly higher than that to the LTS (37%) and the EIS (36%). Although radiosondes are rare and the ERA5 profiles are mostly from the model output over these regions, the EIS$_p$ still provides a much stronger constraint on LCC than LTS and EIS. As shown in Figs. 9d-i through daily to monthly time scales, the EIS$_p$ robustly

explains larger LCC variance than the LTS and EIS especially on short time scales.

(2) *Over midlatitude oceans*, weak and not significant correlations between LCC and the three metrics exist through all of time scales in Fig.9. This poor relationship is also found at the ENA site (Table 2) even using the radiosonde to derive the IS, and thus it is not caused by using the ERA5 to estimate the IS. This suggests that the IS-LCC relationship is indeed not uniform but varies with regions. Klein et al. (2017) also indicated that the LCC relationship with cloud controlling factors (e.g., the IS and sea surface temperature) is systematically different between the subtropical stratocumulus region and other regions (e.g., trade cumulus and midlatitude regions). Thus, when the IS is used to constrain the environmental influence on LCC variations, it should be noted that LCC is not all uniformly constrained by the IS for different regions. For some regions such as midlatitude oceans, the IS might not be a good constraint on LCC. But by more accurately estimating the IS, the $\mathrm{EIS_p}$ is more correlated with LCC than the LTS and EIS over midlatitude oceans such as North Pacific and North Atlantic on all time scales in Figs. 9a-c.

(3) *Over land regions of relatively more LCC (about 15%-25% at south America, China and Europe)*, the correlation between $\mathrm{EIS_p}$ and LCC is comparable to the subtropical oceanic regions through all of time scales in Fig.9. This suggests the $\mathrm{EIS_p}$ is also an important controlling factor for continental LCC over these regions. Besides, the $\mathrm{EIS_p}$ is more correlated with LCC than the LTS and EIS over most land regions, except over China where the LTS explains larger LCC variance than the EIS and $\mathrm{EIS_p}$. The higher correlation of LTS with LCC over China might not be only attributed to the IS (LTS is not a direct measure of inversion but static stability). But more comprehensive and in-depth investigations on the LTS-LCC dependence are needed to understand the exact reason of this phenomenon.

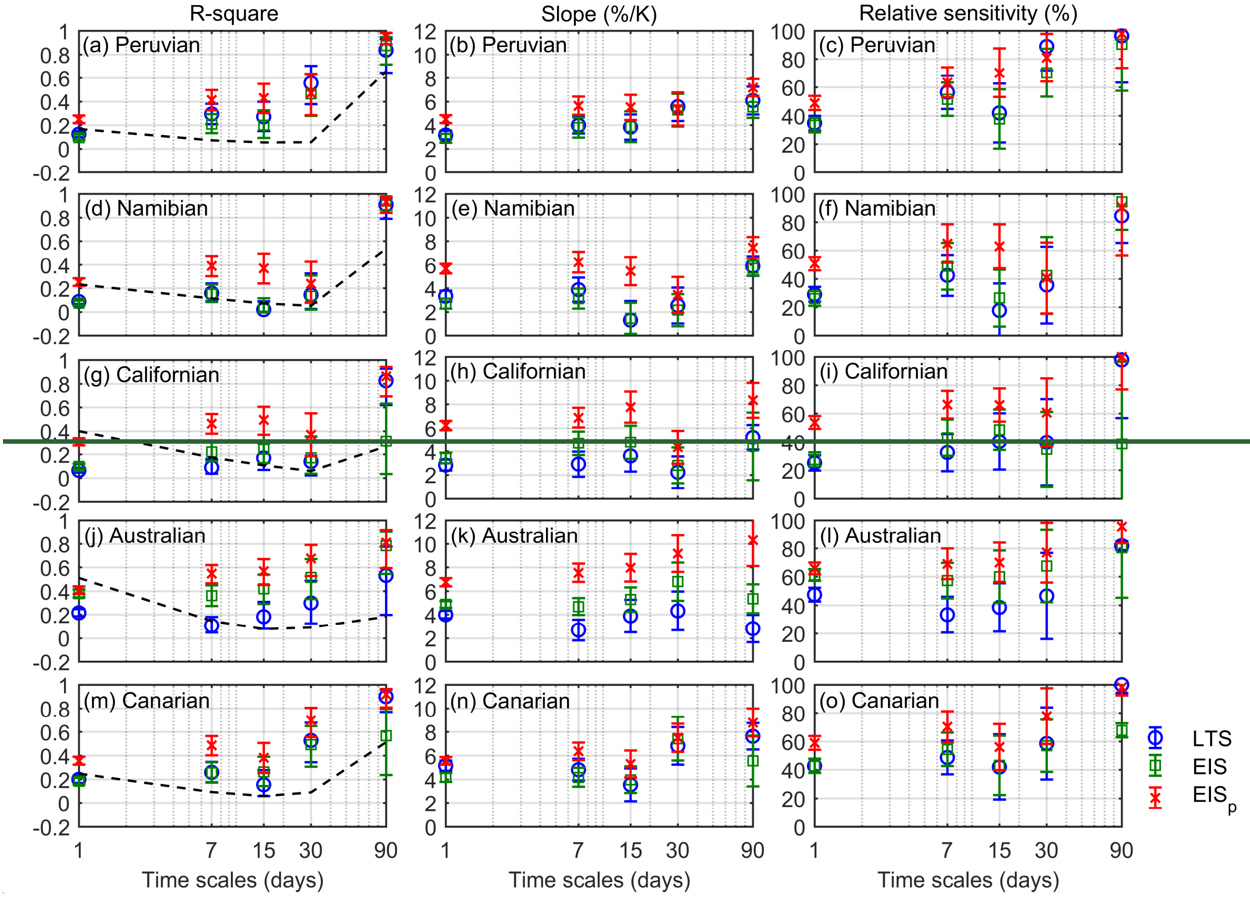

~~On all time scales, the $\mathrm{EIS_p}$ explains larger temporal variance in LCC than the LTS and EIS over most places including those typical low cloud prevailing subtropical eastern oceans (Figs. 9a-c). Over the regions with more than 60% of LCC, the $\mathrm{EIS_p}$ explains 36% of the variance in LCC on average, much larger than that explained by the LTS (21%) and EIS (20%). The mean LCC sensitivity (defined in Eq. (11) and not shown in figure) to the $\mathrm{EIS_p}$ is 48% over these regions, larger than that to the LTS (37%) and EIS (36%). The $\mathrm{EIS_p}$ explains larger LCC variance than the LTS and EIS through all time scales (Figs.~~

~~9d-i).~~

~~Over oceans, the tropical and subtropical LCC is most positively correlated with the three metrics on all of time scales. However, over midlatitude oceans, much weaker or not significant correlations between LCC and the three metrics exist though the annual mean LCC is no less than 40%. The IS and LCC measured by the ARM ENA radiosondes and ground-based instruments also shows a weak IS-LCC correlation (see Table 2) although the ENA site is a midlatitude oceanic site characterized by stratocumulus clouds. This suggests that the IS-LCC relationship is not uniform but varying with regions even over oceans. When the IS is used to constrain the environmental influence on LCC variations, it should be noted that LCC is not all equally constrained by the IS for different regions. For some regions such as midlatitude oceans, the IS might not be a good constraint on LCC. But by more accurately estimating the IS than the LTS and EIS, the EIS_p is more correlated with LCC over either subtropical oceans such as Californian or midlatitude oceans such as North Pacific.~~

~~For land regions with relatively more LCC such as the SGP, China and Russia, the correlation between EIS_p and LCC is comparable to the subtropical oceanic regions through all time scales. This suggests the EIS_p is also an important controlling factor for continental LCC over these regions. Although EIS_p is more correlated with LCC variations than the LTS and EIS over most land regions, over China the LTS explains larger LCC variance than the EIS and EIS_p in Fig. 9a-c. Over China, as shown in Table 2, the LTS-LCC correlation is even larger than the IS-LCC correlation but it is the worst estimation for the IS. This implies that the high correlation of LTS with LCC does not come from the impact of IS controlling LCC but the exact reason behind this is not known.~~

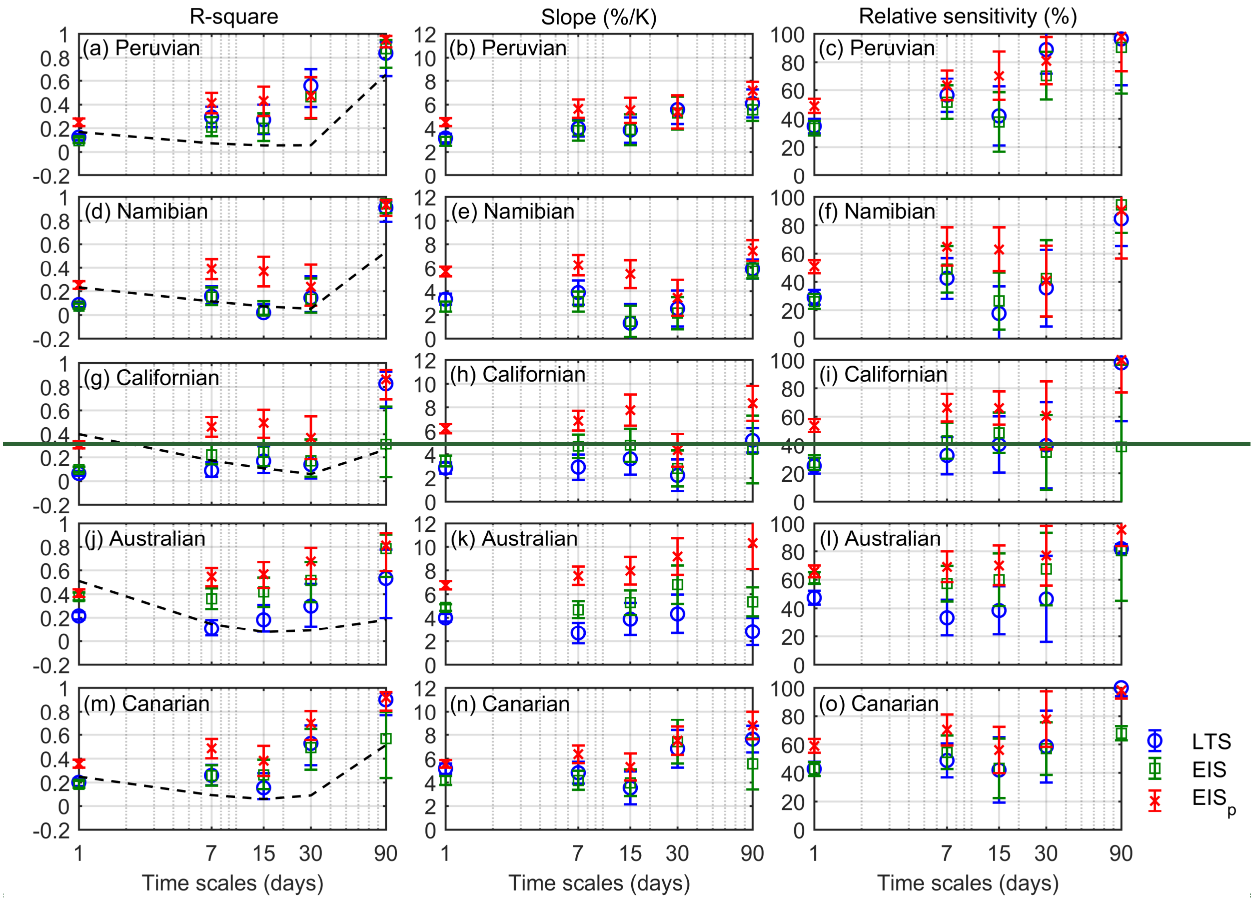

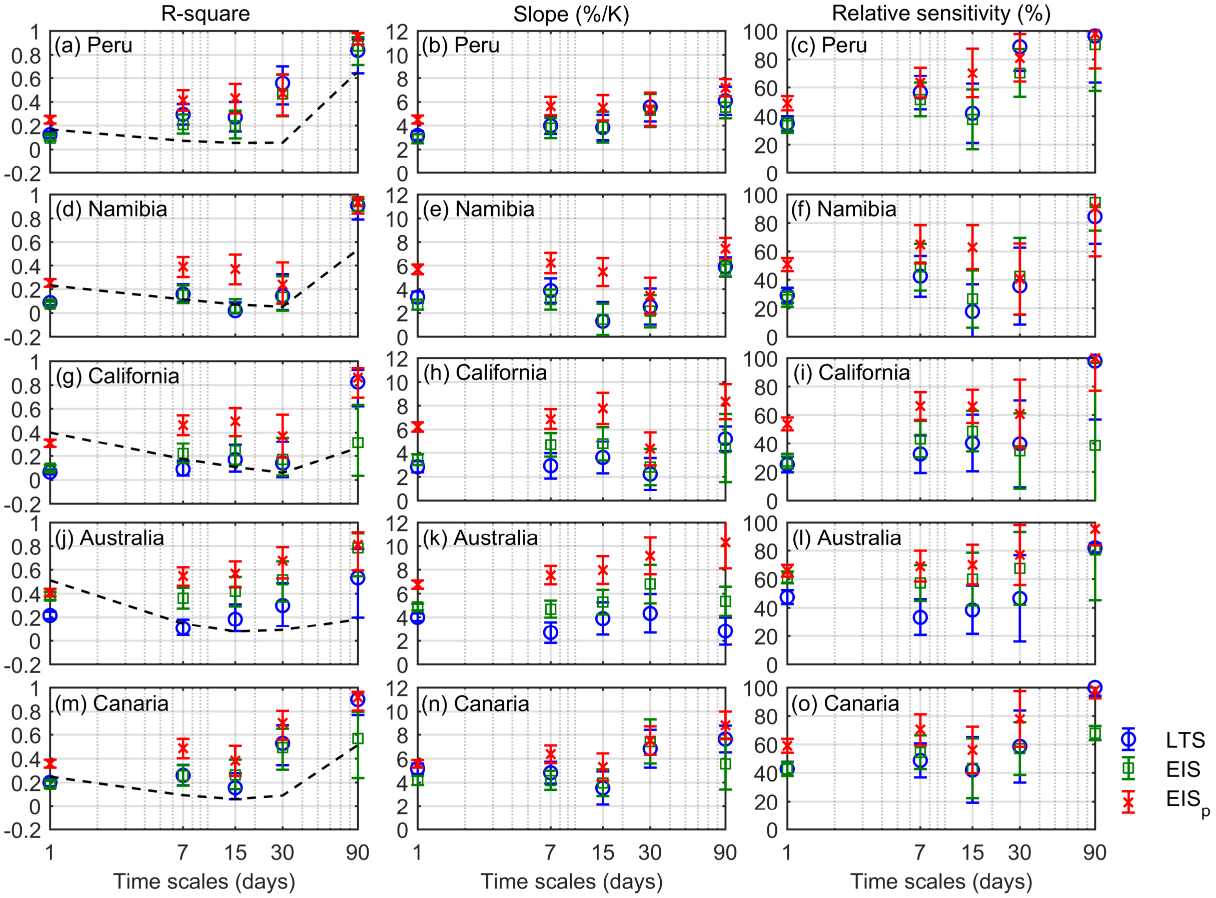

Figure 10. R-square (left panel), slope (middle panel) and relative sensitivity (right panel) of the GEO-MODIS LCC to the ERA5-based 10º×10º regional mean LTS (blue cycle), EIS (green square) and EIS$_p$ (red cross) through daily to seasonal time scales over the five typical eastern oceans defined in Klein and Hartmann (1993). The error bars show the 95% confidence interval based on the t-test. The black dash lines in the left panel are the fraction of the LCC variance on different time scales divided by the total variance.

In Klein and Hartmann (1993), several key low cloud regions are defined. Those regions are of a particular interest in climate projections due to their strong low cloud albedo effects. As shown in Fig. 7, we pick eight key low cloud regions according to Klein and Hartmann [1993] and the linear relationships between LCC and the three metrics are investigated. These regions lack radiosondes for long-term observations of IS. They are separated into a group of five typical tropical and subtropical low cloud prevailing eastern oceans (Fig.10) and a group ~~including~~ of midlatitude oceans and subtropical land (Fig.11).

As shown in Fig. 10 (the dash line in the left panel), over the five key tropical and subtropical eastern oceans, the daily and seasonal window-averaged LCC anomalies accounts for a larger portion of the total LCC variance, indicating the LCC variation mainly happens at the daily and seasonal time scales.~~the LCC variance comes from all of time scales but with relatively larger portions on daily and seasonal time scales.~~ Over the Peruvian, Namibian and Canarian regions, over 50% of LCC variance are from the seasonal variations and much smaller LCC variance is from other four shorter time scales. But over the Californian and Australian regions, 40% and 51% of the LCC variance are from the daily time scale, larger than that on other time scales. Although the LCC variance on the 7-day, 15-day and monthly time scales are relatively smaller, the sum of them still accounts for about 20~30% of the total LCC variance.

In Fig. 10, the LCC variance explained by the LTS, EIS and EIS$_p$ and the LCC slopes of the linear regression ~~composited LCC~~ to them are examined through daily to seasonal time scales. In addition~~Besides~~, the relative LCC sensitivity to those three metrics ~~is defined as~~refers to the LCC sensitivity as defined in Eq. (11) divided by the LCC range. Here the LCC range~~refers to~~ is the difference between the mean values of the largest and the smallest 10% of LCC. The LCC variance is most explained by the EIS$_p$ among the three metrics (left panel of Fig. 10) and LCC is most sensitive to the EIS$_p$ (right panel of Fig. 10) through all of these time scales, except the monthly time scale over the Peruvian region and the seasonal time scale over the Namibian. On the daily time scale, 32% of LCC variance are explained by the EIS$_p$ on average over the five eastern oceans, which is more than twice of the variance explained by the LTS (14%) and EIS (16%). On the longer time scales (30-90 days), overall the EIS$_p$ explains 89% of the LCC seasonal variance on average over the five eastern oceans, in contrast to 80% for the LTS and 70% for the EIS. Only the EIS$_p$ can robustly explain the seasonal variance of LCC exceeding 80% for all locations. However, the EIS cannot well explain the seasonal variation of LCC over the Californian and Canarian regions, and the LTS cannot well explain the seasonal variation of LCC over the Australian region.~~However, the EIS$_p$ robustly explains more than 80% of the seasonal variance in LCC over all places, while the EIS cannot well explain that over the Californian and Canarian regions, as well as the LTS cannot well explain that over the Australian region.~~

It is also noted that the slopes of ~~the composited~~ LCC associated with each metric are not uniform across these key low cloud regions or on different time scales. A similar regional and temporal difference is also found in the LCC-IS relationships (Table 2). Klein et al. (2017) and Szoeke et al. (2016) also found the LCC slopes to the LTS/EIS is variant on different time scales and this time-scale dependence would lead to uncertainties in the final estimates of low-cloud feedbacks. Thus the error estimates of the LCC slopes to the LTS, EIS and EIS$_p$ are needed for the final uncertainty estimates of low-cloud feedbacks. To quantify the relative variation (or the uniformness) of the LCC slope to LTS, EIS and EIS$_p$, we compute the ratio between the standard deviation and the mean of grouped slopes. For the temporal relative variation, over each region slopes on different time scales are grouped together. While for the regional relative variation, on each time scale slopes over different regions are grouped together. The temporal relative variation of the LCC slope to the LTS and EIS is 32% and 29% on average over the five eastern oceans. In contrast, the temporal relative variation of the LCC slope to the EIS$_p$ is 21%. Besides, the regional relative variation of the LCC slope to the LTS, EIS and EIS$_p$ is 24%, 21% and 18% between the five eastern oceans, respectively. This suggests that the regional/temporal dependence of the LCC slope in the estimate of low cloud feedbacks is also non-negligible and needs to be considered in the final error estimates or to estimate low-cloud feedbacks by separating regions.

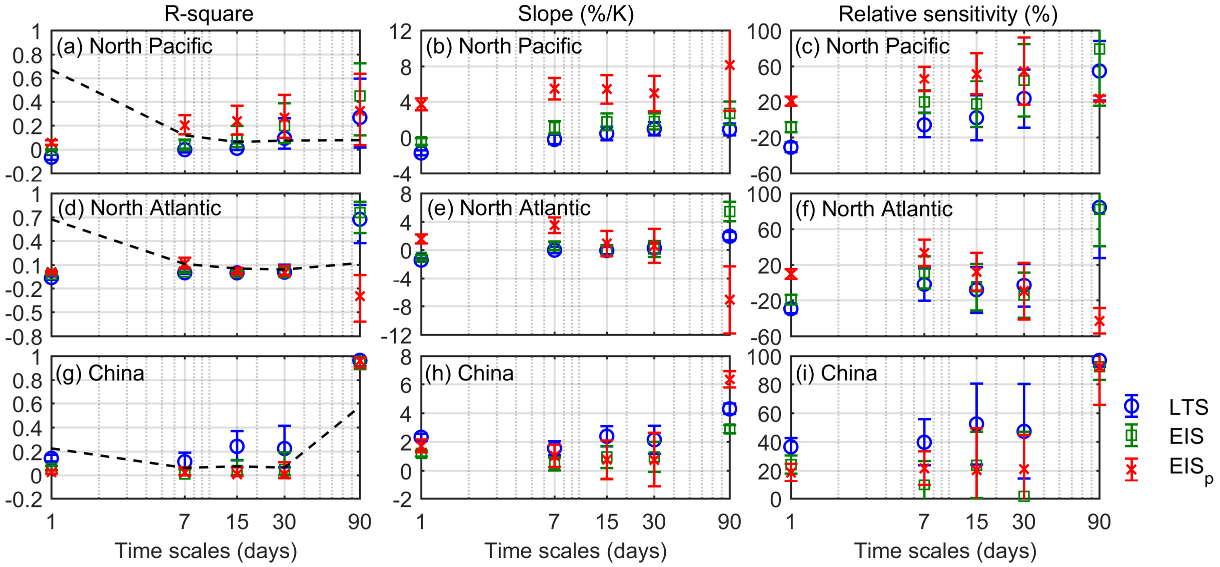

Figure 11. Similar to Fig. 10 but for the other three regions defined in Klein and Hartmann (1993), including two midlatitude oceans and one subtropical land. The minus/plus sign of R-square indicates negative/positive correlations.

Figs. 11a and 11d (the dash line) show that over the North Pacific and North Atlantic regions, 67% of the LCC variance is from the daily time scale~~variance from the daily time scale dominates (67%)~~, while over the China region in Fig.11g, variance is mostly from the seasonal time scale ~~is the largest~~ (57%~~, Fig.11g~~). Over the North Pacific and North Atlantic regions, LCC is not necessarily correlated with the IS. Norris (1998) has found that fogs and bad-weather stratus clouds frequently occur over the midlatitude ocean but with less inversions and poor IS-LCC relationships. Similarly, poor correlation (Figs. 11a and 11d) and sensitivity (Figs. 11c and 11f) between LCC and LTS/EIS/EIS$_p$ are found over the North Pacific and North Atlantic. But, the EIS$_p$ is closest to the radiosonde-detected IS as compared with the LTS and EIS at the ENA and OWS C as shown in Table 2. This suggests that the EIS$_p$ is still a reliable estimation for the IS to represent the true IS-LCC relationship. But the LTS/EIS-LCC relationship is not necessarily due to the IS influence on LCC. Figs. 11a, 11d, 11c and 11f also show that the LTS/EIS-LCC correlation and sensitivity is very different from that between LCC and EIS$_p$ on the daily and seasonal time scales. Unfortunately, it has not been well explored about the midlatitude LCC-IS relationship. The poor EIS$_p$-LCC relationship represents that the IS cannot be a cloud controlling factor as important as that over subtropical oceans.~~limited knowledge about why this happen is known. The poor EIS$_p$-LCC relationship represents that the IS cannot be a cloud controlling factor as important as that over subtropical oceans.~~ Over the Chinese region, the EIS and EIS$_p$ are both better correlated with the IS as shown in Table 2. Fig. 11g and Fig. 11i shows that LCC is slightly more corelated with and sensitive to the LTS through all time scales. These higher correlations and sensitivity are not related to the IS since the LTS correlates the least with the IS~~is the worst estimation for the IS~~. Since the LTS not just includes the IS but actually represents the total static stability from 1000hPa to 700hPa to influence the amount and liquid water path of low clouds (Klein and Hartmann, 1993; Kawai and Teixeira, 2010),~~But~~ it may imply that there are other thermal factors ~~except~~ in addition to the IS ~~counted into~~in LTS to contribute to these higher correlations and sensitivity. Overall, it should be noted that the IS may not be a strong cloud-controlling factor over the midlatitude oceans and subtropical land but EIS$_p$ is still the best estimation for the IS. The IS is not the only LCC controlling factor, and other factors (e.g., sea surface temperature, cold advection, free-tropospheric humidity and vertical velocity) are also important for influencing LCC (Myers and Norris, 2013; Klein et al., 2017).

All above analyses (Figs. ~~7~~8-11) are based on the daily-averaged LTS, EIS and EIS$_p$ data, which are computed based on the 3-hour 1° ERA5 atmospheric profiles. Based on the monthly mean atmospheric profiles, over the region of LCC larger than 60%, the LTS and EIS explain 50% and 48% of LCC variance, which is similar to the value of 53% based on the 3-hour ERA5 atmospheric profiles. However, the EIS$_p$ based on the monthly mean ERA5 profiles explains 49% of the LCC variance, which is significantly lower than the 65% based on the 3-hour profiles. Thus for accurately computing the EIS$_p$ on either short or long timescales, high temporal resolution of reanalysis data is necessary.

5. Conclusion

In this paper, a novel profile-based estimated IS (EIS$_p$) is developed based on the thinnest possible layer that contains the inversion layer in the ERA5 profiles. By this method, the effects of the static stability below the LCL are completely removed. The errors due to the spread of the environmental θ gradient around the moist adiabat above the LCL are reduced.

At the ARM SGP site, the EIS$_p$ more accurately estimates the IS, with a correlation of 0.74, than the LTS (0.53) and EIS (0.45). Thus, the EIS$_p$ reasonably replicates the constraints of IS on the PBL moisture distribution and LCC, while the LTS/EIS has a weak/~~wrong~~ erroneous relationship with the PBL moisture and LCC. The LCC sensitivity to LTS and EIS and EIS$_p$ is 39%, 12% and 50%, respectively. On the daily time scale (7-day mean excluded), the variance in LCC explained by the EIS$_p$ (9.1%) is more than twice that explained by both the LTS (3.1%) and EIS (-0.4%). At the ARM ENA site, the EIS$_p$ has similar advantages on estimating the IS. At other available oceanic and coastal observation stations, the EIS$_p$ is still a better estimation for the IS than the LTS and EIS.

At the global scale, according to the GEO-MODIS LCC observations, the EIS$_p$ better explains the spatial and temporal variations of LCC than the LTS and EIS. Over oceans, the EIS$_p$ distribution is more consistent with the LCC pattern compared with the LTS and EIS. The locations of the strongest EIS$_p$ are consistent with the centers of the largest LCC relatively away from the coast, while the centers of the strongest LTS and EIS are over the coast. Over the subtropical LCC domains, the LCC sensitivity to the EIS$_p$ is 48%, larger than that to the LTS (37%) and EIS (36%) on all time scales. And the increased LCC sensitivity to EIS_p primarily comes from time scales shorter than a month. Over the typical low-cloud prevailing eastern oceans as defined in Klein and Hartmann (1993), the LCC daily variance explained by the EIS_p is 32% and twice that explained by the LTS/EIS. And the LCC seasonal variance explained by the EIS_p increases to 89% as compared with that explained by the LTS (80%) and EIS (70%).

No uniform relationship between the LCC and any of the IS, LTS, EIS and EIS_p is found across time scales or different regions. As compared to the LTS/EIS, the temporal relative variation of the LCC slopes to the EIS_p is reduced from 32%/29% to 21%. The regional relative variation of the LCC slope to the EIS_p is slightly smaller than that of LTS and EIS. This non-uniform~~ness of the~~ LCC sensitivity to ~~the IS~~cloud controlling factors across different regions and time scales suggests that using a single observational multi-linear regression between LCC and cloud-controlling factors to estimate the global low cloud feedbacks is not recommended.~~ and three metrices suggests that the estimate of low cloud feedbacks based on a single observed relationship is questionable.~~

Overall, the EIS_p is an improved measure of the IS and better constrains LCC, especially on time scales shorter than a month. On short time scales, the enhanced dependence of LCC on the EIS_p makes the EIS_p more suitable to resolve process-oriented studies associated with LCC variations. Therefore, the EIS_p is likely a better constraint to reduce the meteorological covariations to separate the aerosol effects in aerosol-cloud interactions.

Author contribution.

JY and RW designed the experiments and ZW carried them out. JY and ZW prepared the first version of the manuscript with contributions from all co-authors. YC prepared the ERA5 data and TT inspected some individual profiles and cloud images. All authors verified the final version of the manuscript.

Competing interests.

The authors declare that they have no conflict of interest.

Acknowledgment

This work was supported by the NSFC-41875004 and the National Key R&D Program of China (2016YFC0202000). The first author thanks the “Double First-class” initiative program providing an opportunity for him to visit and study at the University of Washington.

Data Availability Statement

All data used in this study are available online. The ARM SGP and ENA radiosonde and cloud data were obtained from the ARM Research Facility and are available at https://www.arm.gov. The IGRA radiosondes are available from the NOAA National Centers for Environmental Information at https://www.ncei.noaa.gov/products/weather-balloon/integrated-global-radiosonde-archive. The GEO-MODIS LCC product is provided by the NASA Langley Research Center at https://earthdata.nasa.gov. The ERA5 reanalysis used in this study is from the ECMWF and available at https://cds.climate.copernicus.eu/cdsapp#!/home.

Reference

Ackerman, T. P. and Stokes, G. M.: The Atmospheric Radiation Measurement Program, Physics Today, 56, 38-44, 10.1063/1.1554135, 2003.

Albrecht, B. A., Jensen, M. P., and Syrett, W. J.: Marine boundary layer structure and fractional cloudiness, Journal of Geophysical Research, 100, 10.1029/95jd00827, 1995.

Bretherton, C. S. and Wyant, M. C.: Moisture Transport, Lower-Tropospheric Stability, and Decoupling of Cloud-Topped Boundary Layers, Journal of the Atmospheric Sciences, 54, 148-167, 10.1175/1520-0469(1997)054<0148:Mtltsa>2.0.Co;2, 1997.

Bretherton, C. S., Widmann, M., Dymnikov, V. P., Wallace, J. M., and Bladé, I.: The Effective Number of Spatial Degrees of Freedom of a Time-Varying Field, Journal of Climate, 12, 1990-2009, 10.1175/1520-0442(1999)012<1990:Tenosd>2.0.Co;2, 1999.

Bretherton, C. S., Uttal, T., Fairall, C. W., Yuter, S. E., Weller, R. A., Baumgardner, D., Comstock, K., Wood, R., and Raga, G. B.: The Epic 2001 Stratocumulus Study, Bulletin of the American Meteorological Society, 85, 967-978, 10.1175/bams-85-7-967, 2004.

Chen, X. and Xie, S.: ARM Best Estimate Data Products (ARMBECLDRAD), Atmospheric Radiation Measurement (ARM) user facility, 10.5439/1333228, 1996.

Coopman, Q., Garrett, T. J., Riedi, J., Eckhardt, S., and Stohl, A.: Effects of long-range aerosol transport on the microphysical properties of low-level liquid clouds in the Arctic, Atmospheric Chemistry and Physics, 16, 4661-4674, 10.5194/acp-16-4661-2016, 2016.

Cutler, L., Brunke, M. A., and Zeng, X.: Re-Evaluation of Low Cloud Amount Relationships With Lower-Tropospheric Stability and Estimated Inversion Strength, Geophysical Research Letters, 49, 10.1029/2022gl098137, 2022.

Doelling, D. R., Sun, M., Nguyen, L. T., Nordeen, M. L., Haney, C. O., Keyes, D. F., and Mlynczak, P. E.: Advances in Geostationary-Derived Longwave Fluxes for the CERES Synoptic (SYN1deg) Product, Journal of Atmospheric and Oceanic Technology, 33, 503-521, 10.1175/jtech-d-15-0147.1, 2016.

Doelling, D. R., Loeb, N. G., Keyes, D. F., Nordeen, M. L., Morstad, D., Nguyen, C., Wielicki, B. A., Young, D. F., and Sun, M.: Geostationary Enhanced Temporal Interpolation for CERES Flux Products %J Journal of Atmospheric and Oceanic Technology, 30, 1072-1090, 10.1175/jtech-d-12-00136.1, 2013.

Dong, X. Q., Minnis, P., and Xi, B. K.: A climatology of midlatitude continental clouds from the ARM SGP Central Facility: Part I: Low-level cloud macrophysical, microphysical, and radiative properties, Journal of Climate, 18, 1391-1410, Doi 10.1175/Jcli3342.1, 2005.

Durre, I., Vose, R. S., and Wuertz, D. B.: Overview of the Integrated Global Radiosonde Archive, Journal of Climate, 19, 53-68, Doi 10.1175/Jcli3594.1, 2006.

Durre, I., Yin, X., Vose, R. S., Applequist, S., and Arnfield, J.: Enhancing the Data Coverage in the Integrated Global Radiosonde Archive, Journal of Atmospheric and Oceanic Technology, 35, 1753-1770, 10.1175/jtech-d-17-0223.1, 2018.

Gryspeerdt, E., Quaas, J., and Bellouin, N.: Constraining the aerosol influence on cloud fraction, Journal of Geophysical Research: Atmospheres, 121, 3566-3583, 10.1002/2015jd023744, 2016.

Hersbach, H., Bell, B., Berrisford, P., Hirahara, S., Horányi, A., Muñoz-Sabater, J., Nicolas, J., Peubey, C., Radu, R., Schepers, D., Simmons, A., Soci, C., Abdalla, S., Abellan, X., Balsamo, G., Bechtold, P., Biavati, G., Bidlot, J., Bonavita, M., Chiara, G., Dahlgren, P., Dee, D., Diamantakis, M., Dragani, R., Flemming, J., Forbes, R., Fuentes, M., Geer, A., Haimberger, L., Healy, S., Hogan, R. J., Hólm, E., Janisková, M., Keeley, S., Laloyaux, P., Lopez, P., Lupu, C., Radnoti, G., Rosnay, P., Rozum, I., Vamborg, F., Villaume, S., and Thépaut, J. N.: The ERA5 global reanalysis, Quarterly Journal of the Royal Meteorological Society, 146, 1999-2049, 10.1002/qj.3803, 2020.

Jones, C. R., Bretherton, C. S., and Leon, D.: Coupled vs. decoupled boundary layers in VOCALS-REx, Atmospheric Chemistry and Physics, 11, 7143-7153, 10.5194/acp-11-7143-2011, 2011.

Kawai, H. and Teixeira, J.: Probability Density Functions of Liquid Water Path and Cloud Amount of Marine Boundary Layer Clouds: Geographical and Seasonal Variations and Controlling Meteorological Factors, Journal of Climate, 23, 2079-2092, 10.1175/2009jcli3070.1, 2010.

Kawai, H., Koshiro, T., and Webb, M. J.: Interpretation of Factors Controlling Low Cloud Cover and Low Cloud Feedback Using a Unified Predictive Index, Journal of Climate, 30, 9119-9131, 10.1175/jcli-d-16-0825.1, 2017.

Ken, B.: Balloon-Borne Sounding System (SONDEWNPN), Atmospheric Radiation Measurement (ARM) user facility, https://doi.org/10.5439/1595321, 2001.

Klein, S. A.: Synoptic Variability of Low-Cloud Properties and Meteorological Parameters in the Subtropical Trade Wind

Boundary Layer, Journal of Climate, 10, 2018-2039, 10.1175/1520-0442(1997)010<2018:Svolcp>2.0.Co;2, 1997.

Klein, S. A. and Hartmann, D. L.: The Seasonal Cycle of Low Stratiform Clouds, Journal of Climate, 6, 1587-1606, 10.1175/1520-0442(1993)006<1587:Tscols>2.0.Co;2, 1993.

Klein, S. A., Hartmann, D. L., and Norris, J. R.: On the Relationships among Low-Cloud Structure, Sea Surface Temperature, and Atmospheric Circulation in the Summertime Northeast Pacific, Journal of Climate, 8, 1140-1155, 10.1175/1520-0442(1995)008<1140:Otralc>2.0.Co;2, 1995.

Klein, S. A., Hall, A., Norris, J. R., and Pincus, R.: Low-Cloud Feedbacks from Cloud-Controlling Factors: A Review, Surveys in Geophysics, 38, 1307-1329, 10.1007/s10712-017-9433-3, 2017.

L'Ecuyer, T. S., Berg, W., Haynes, J., Lebsock, M., and Takemura, T.: Global observations of aerosol impacts on precipitation occurrence in warm maritime clouds, Journal of Geophysical Research, 114, 10.1029/2008jd011273, 2009.

Li, J., Yi, Y., Minnis, P., Huang, J., Yan, H., Ma, Y., Wang, W., and Kirk Ayers, J.: Radiative effect differences between multi-layered and single-layer clouds derived from CERES, CALIPSO, and CloudSat data, Journal of Quantitative Spectroscopy and Radiative Transfer, 112, 361-375, 10.1016/j.jqsrt.2010.10.006, 2011.

Liu, S. Y. and Liang, X. Z.: Observed Diurnal Cycle Climatology of Planetary Boundary Layer Height, Journal of Climate, 23, 5790-5809, 10.1175/2010jcli3552.1, 2010.

Mauger, G. S. and Norris, J. R.: Meteorological bias in satellite estimates of aerosol-cloud relationships, Geophysical Research Letters, 34, 10.1029/2007gl029952, 2007.

Mauger, G. S. and Norris, J. R.: Assessing the Impact of Meteorological History on Subtropical Cloud Fraction, Journal of Climate, 23, 2926-2940, 10.1175/2010jcli3272.1, 2010.

McCoy, D. T., Eastman, R., Hartmann, D. L., and Wood, R.: The Change in Low Cloud Cover in a Warmed Climate Inferred from AIRS, MODIS, and ERA-Interim, Journal of Climate, 30, 3609-3620, 10.1175/jcli-d-15-0734.1, 2017.

Minnis, P., Trepte, Q. Z., Sun-Mack, S., Chen, Y., Doelling, D. R., Young, D. F., Spangenberg, D. A., Miller, W. F., Wielicki, B. A., Brown, R. R., Gibson, S. C., and Geier, E. B.: Cloud Detection in Nonpolar Regions for CERES Using TRMM VIRS and Terra and Aqua MODIS Data, IEEE Transactions on Geoscience and Remote Sensing, 46, 3857-3884, 10.1109/tgrs.2008.2001351, 2008.

Minnis, P., Sun-Mack, S., Young, D. F., Heck, P. W., Garber, D. P., Chen, Y., Spangenberg, D. A., Arduini, R. F., Trepte, Q. Z., Smith, W. L., Ayers, J. K., Gibson, S. C., Miller, W. F., Hong, G., Chakrapani, V., Takano, Y., Liou, K.-N., Xie, Y., and Yang, P.: CERES Edition-2 Cloud Property Retrievals Using TRMM VIRS and Terra and Aqua MODIS Data—Part I: Algorithms, IEEE Transactions on Geoscience and Remote Sensing, 49, 4374-4400, 10.1109/tgrs.2011.2144601, 2011.

Mohrmann, J., Bretherton, C. S., McCoy, I. L., McGibbon, J., Wood, R., Ghate, V., Albrecht, B., Sarkar, M., Zuidema, P., and Palikonda, R.: Lagrangian Evolution of the Northeast Pacific Marine Boundary Layer Structure and Cloud during CSET, Monthly Weather Review, 147, 4681-4700, 10.1175/mwr-d-19-0053.1, 2019.

Murray-Watson, R. J. and Gryspeerdt, E.: Stability-dependent increases in liquid water with droplet number in the Arctic, Atmospheric Chemistry and Physics, 22, 5743-5756, 10.5194/acp-22-5743-2022, 2022.

Myers, T. A. and Norris, J. R.: Observational Evidence That Enhanced Subsidence Reduces Subtropical Marine Boundary Layer Cloudiness, Journal of Climate, 26, 7507-7524, 10.1175/jcli-d-12-00736.1, 2013.

Myers, T. A. and Norris, J. R.: Reducing the uncertainty in subtropical cloud feedback, Geophysical Research Letters, 43, 2144-2148, 10.1002/2015gl067416, 2016.

Myers, T. A., Scott, R. C., Zelinka, M. D., Klein, S. A., Norris, J. R., and Caldwell, P. M.: Observational constraints on low cloud feedback reduce uncertainty of climate sensitivity, Nature Climate Change, 11, 501-507, 10.1038/s41558-021-01039-0, 2021.

Nicholls, S.: The dynamics of stratocumulus: Aircraft observations and comparisons with a mixed layer model, Quarterly Journal of the Royal Meteorological Society, 110, 783-820, 10.1002/qj.49711046603, 1984.

Norris, J. R.: Low Cloud Type over the Ocean from Surface Observations. Part I: Relationship to Surface Meteorology and the Vertical Distribution of Temperature and Moisture, Journal of Climate, 11, 369-382, 10.1175/1520-0442(1998)011<0369:Lctoto>2.0.Co;2, 1998.

Park, S. and Shin, J.: Heuristic estimation of low-level cloud fraction over the globe based on a decoupling parameterization, Atmospheric Chemistry and Physics, 19, 5635-5660, 10.5194/acp-19-5635-2019, 2019.

Qu, X., Hall, A., Klein, S. A., and Caldwell, P. M.: The strength of the tropical inversion and its response to climate change in 18 CMIP5 models, Clim Dynam, 45, 375-396, 10.1007/s00382-014-2441-9, 2014.

Romps, D. M.: Exact Expression for the Lifting Condensation Level, Journal of the Atmospheric Sciences, 74, 3891-3900, 10.1175/jas-d-17-0102.1, 2017.

Rosenfeld, D., Zhu, Y., Wang, M., Zheng, Y., Goren, T., and Yu, S.: Aerosol-driven droplet concentrations dominate coverage and water of oceanic low-level clouds, Science, 363, 10.1126/science.aav0566, 2019.

Schneider, T. and O’Gorman, P. A.: Moist Convection and the Thermal Stratification of the Extratropical Troposphere, Journal of the Atmospheric Sciences, 65, 3571-3583, 10.1175/2008jas2652.1, 2008.

Seethala, C., Norris, J. R., and Myers, T. A.: How Has Subtropical Stratocumulus and Associated Meteorology Changed since the 1980s?*, Journal of Climate, 28, 8396-8410, 10.1175/jcli-d-15-0120.1, 2015.

Sherwood, S. C., Webb, M. J., Annan, J. D., Armour, K. C., Forster, P. M., Hargreaves, J. C., Hegerl, G., Klein, S. A., Marvel, K. D., Rohling, E. J., Watanabe, M., Andrews, T., Braconnot, P., Bretherton, C. S., Foster, G. L., Hausfather, Z., von der Heydt, A. S., Knutti, R., Mauritsen, T., Norris, J. R., Proistosescu, C., Rugenstein, M., Schmidt, G. A., Tokarska, K. B., and Zelinka, M. D.: An Assessment of Earth's Climate Sensitivity Using Multiple Lines of Evidence, Rev Geophys, 58, e2019RG000678, 10.1029/2019RG000678, 2020.

Stevens, B. and Brenguier, J.-L.: Cloud-controlling factors: Low clouds, 2009.

Stone, P. H.: A Simplified Radiative-Dynamical Model for the Static Stability of Rotating Atmospheres, Journal of the Atmospheric Sciences, 29, 405-418, 10.1175/1520-0469(1972)029<0405:Asrdmf>2.0.Co;2, 1972.

Szoeke, S. P., Verlinden, K. L., Yuter, S. E., and Mechem, D. B.: The Time Scales of Variability of Marine Low Clouds, Journal of Climate, 29, 6463-6481, 10.1175/jcli-d-15-0460.1, 2016.

Trepte, Q. Z., Bedka, K. M., Chee, T. L., Minnis, P., Sun-Mack, S., Yost, C. R., Chen, Y., Jin, Z., Hong, G., Chang, F.-L., and Smith, W. L.: Global Cloud Detection for CERES Edition 4 Using Terra and Aqua MODIS Data, IEEE Transactions on Geoscience and Remote Sensing, 57, 9410-9449, 10.1109/tgrs.2019.2926620, 2019.

Webb, M. J., Lambert, F. H., and Gregory, J. M.: Origins of differences in climate sensitivity, forcing and feedback in climate models, Clim Dynam, 40, 677-707, 10.1007/s00382-012-1336-x, 2012.

Wood, R. and Bretherton, C. S.: Boundary Layer Depth, Entrainment, and Decoupling in the Cloud-Capped Subtropical and Tropical Marine Boundary Layer, Journal of Climate, 17, 3576-3588, 10.1175/1520-0442(2004)017<3576:Bldead>2.0.Co;2, 2004.

Wood, R. and Bretherton, C. S.: On the Relationship between Stratiform Low Cloud Cover and Lower-Tropospheric Stability, Journal of Climate, 19, 6425-6432, 10.1175/jcli3988.1, 2006.